Continuum-level modeling of Li-ion battery SEI by upscaling atomistically informed reaction mechanisms

Peter J. Weddle[a,∗], Evan Walter Clark Spotte-Smith[b,c], Ankit Verma[a], Hetal D. Patel[b,c],
Kae Fink[a], Bertrand J. Tremolet de Villers[a], Maxwell C. Schulze[a], Samuel M. Blau[d],
Kandler A. Smith[a], Kristin A. Persson[b,e], Andrew M. Colclasure[a]

[a]*National Renewable Energy Laboratory (NREL), 15013 Denver West Parkway, Golden, CO 80401, USA*
[b]*Department of Materials Science and Engineering, University of California, Berkeley, CA 94720, USA*
[c]*Materials Science Division, Lawrence Berkeley National Laboratory, Berkeley, CA 94720, USA*
[d]*Energy Technologies Area, Lawrence Berkeley National Laboratory, Berkeley, CA 94720, USA*
[e]*Molecular Foundry, Lawrence Berkeley National Laboratory, Berkeley, CA 94720, USA*

Abstract

Understanding and controlling solid-electrolyte interphase (SEI) formation to stabilize cell performance is a significant challenge for next-generation Li-ion battery technologies. In recent years, computational modeling has become an essential tool in providing fundamental insights into SEI properties and dynamics. However, neither atomistic nor continuum-level approaches alone can capture the complexities of SEI chemistry across all relevant length and time scales. In this work, a continuum-level model is developed that is informed by reaction mechanisms obtained from first-principle calculations. The atomistically informed continuum-level model is used to understand electrolyte degradation, including the decomposition of ethylene carbonate (EC), ethyl methyl carbonate (EMC), and fluoroethylene carbonate (FEC). The model presented here is the most chemically complex continuum-level SEI model in the literature to date. The SEI model is calibrated against experimental irreversible leakage currents and shows qualitative agreement with expected SEI growth trends. The model framework is expected to accelerate fundamental understanding of SEI formation, facilitate mechanism development feedback, and dynamically interact with experimental insights.

Keywords: Lithium-ion battery, Silicon anode, solid-electrolyte interphase, continuum-level model

1. Introduction

Lithium-ion batteries are the energy storage solution of choice for consumer electronics and are increasingly important for transportation (e.g., electric vehicles) [1]. For Li-ion batteries to expand use in transportation and new applications such as grid-scale energy storage, chemistries with higher energy densities are needed. However, energy-dense Li-ion batteries suffer from inherent instability. Common electrolytes based on Li salts (e.g. lithium hexafluorophosphate or $LiPF_6$) dissolved in carbonate solvents (e.g., ethylene carbonate or EC and ethyl methyl carbonate or EMC) have limited electrochemical stability windows and are thermodynamically unstable at the plating potential of

Li metal, the intercalation potentials of anodes made of graphite and silicon, and the intercalation potentials of some high-voltage cathodes [2–5].

When Li-ion electrolytes are exposed to potentials outside of their electrochemical stability windows, the electrolyte molecules degrade via parasitic side reactions. These side reactions commonly lead to the formation of nanoscale passivation films known as solid electrolyte interphase (SEI) layers [6]. Long-term Li-ion battery life is directly related to the formation of SEI on the electrochemically unstable electrode surface [2, 7, 8]. Ideally, the SEI, after formation, would stop growing and prevent additional Li-ion consumption and electrolyte degradation. However, in practice, SEI layers are not stagnant; SEI composition, structure, and thickness can change during cycling and calendar aging [9–12]. Continual SEI formation can result in battery failure due to loss of lithium inventory, electrolyte

---
∗Corresponding author. Tel: (303) 275-4739.
Email address: `peter.weddle@nrel.gov` (Peter J. Weddle)

dry-out, and increased cell impedance [13]. Thus, an understanding of SEI formation and its resultant properties is needed to ensure long-term battery life.

In the case of graphite, SEI formation procedures and electrolyte additives have been adequately designed to such an extent that extremely long life-times are possible [3, 14]. On the other hand, Si and its oxide variants suffer from continuous SEI-forming side reactions, resulting in rapid cell failure especially in terms of calendar life [15–17]. Silicon's primary failure mechanism is commonly argued to be self-pulverization due to its significant volume change on cycling [18–20]. To this end, novel designs have been used to reduce the Si-particle self-pulverization [21]; for example, by reducing the Si particle size to less than a micrometer. However, cycling and calendar-life studies indicate that despite novel particle and electrode structuring to account for Si volume expansion, the SEI on Si in carbonate electrolytes is inherently non-passivating, which results in short calendar life (order 2 years) [12, 15, 17, 22].

To increase Li-ion battery lifetimes, a primary goal of the research community is to engineer SEI layers that have 1) improved electronic passivation, 2) increased ionic conductivity, and 3) increased mechanical robustness to ensure good adhesion to the anode surface. These improvements are especially important for next-generation electrodes (e.g., Si and Li metal). Designing an optimal SEI requires knowledge of its chemically complex formation process, long-term stability, and dependencies on electrode, electrolyte composition [3, 15, 23, 24], additives [16, 25–27], operating temperature [26, 27], formation rate [28], formation voltage hold [29, 30], functional termination state [31, 32], and formation time [3]. Such a task is extremely challenging [33], and fundamental knowledge gaps regarding the SEI remain even after decades of dedicated study.

With the aim to assist in understanding and designing better SEI layers, the present manuscript discusses a continuum-level modeling approach that communicates fundamental insights from the atomistic scale to length- and time-scales relevant to experimentally measurable signals. First, a short review of previous modeling approaches is provided to highlight the uniqueness, advantages, and disadvantages of the proposed approach. A review on experimental techniques is not provided but can be found elsewhere [3, 8, 10, 13]. Following this review, a continuum-level single-particle model is developed to study SEI formation on a Si nanoparticle. The model includes reaction mechanisms for the decomposition of EC, EMC, and fluoroethylene carbonate (FEC) to form common SEI components (e.g., lithium fluoride

or LiF, lithium carbonate or Li_2CO_3, and lithium ethylene dicarbonate or LEDC) and gas products (e.g., CO, CO_2, CH_4, C_2H_6), with energy barriers and rate constants obtained using density functional theory (DFT), transition state theory, and Marcus theory. The model is calibrated using irreversible leakage currents from voltage-hold experiments [17, 22, 34–37].

The model presented here is by far the most chemically complex continuum model describing SEI formation ever reported in the literature in terms of both the number of species and the number of reactions considered. However, just as important as documenting the current model is the possibility of further developments; the model is carefully designed such that it can be modified and expanded to capture yet more complex reactivity and aid in the practical design of SEI layers.

1.1. Atomistic-level models

Atomistic modeling is well suited to identify fundamental reaction and transport mechanisms in battery environments [38], which often cannot be directly observed in experimental characterization [39]. Due to its balance of computational cost and accuracy, DFT has long been the quantum chemical method of choice for predicting reduction potentials [40], reaction thermodynamics, and kinetics [41, 42]. Conventional DFT studies of electrolyte decomposition and SEI formation are conducted in a low-throughput mode [43–45], where individual reaction pathways are constructed by hand and based on human intuition. More recently, chemical reaction networks (CRNs) have been developed to automatically predict likely decomposition products [46, 47] and automatically suggest chemically plausible reaction pathways to a large numbers of species [48–50], bringing a thorough exploration of battery reactivity closer to reality.

Even with advanced high-throughput and data-driven methods, DFT alone cannot capture competition between different reaction pathways or the dynamics of SEI formation and growth. Molecular dynamics (MD) can overcome this limitation to a certain extent, by predicting a time- and space-resolved picture of electrolyte reactivity. Though useful for simulating mass [51] and charge transport [52] and simulating reactivity in an unbiased manner [53], MD methods are severely limited by time scale. When classical reactive force-fields are used to generate forces and determine molecular motion, MD can readily simulate up to ≈ 100 ns; when *ab initio* methods like DFT are used, the accessible time scale is only ≈ 10 ps. This means that MD methods can only simulate the very early stages of SEI formation [54].

Microkinetic models using kinetic Monte Carlo (kMC) methods can bridge the gap between the atomistic and the nanoscale. These kMC models can capture both reactivity and transport, while abstracting away from an all-atom to a (typically) molecule-scale or even more granular representation [55]. Though most kMC studies of the SEI have involved very few species and reactions and have relied on arbitrary or fitted reaction rates [56, 57], it is possible to develop models with complex reaction mechanisms (for instance, based on CRN analysis) that can simulate up to the ≈ 1 s time scale and can reproduce and explain compositional trends in the SEI [50]. However, even with appropriate acceleration techniques, these microkinetic models struggle to access the time scales necessary to understand SEI growth, evolution, and aging (especially calendar aging), which motivates the upscaling of atomistic-level inputs to continuum-level models.

1.2. Continuum-level models

There are two phenomenological continuum-level models for the SEI. The first model, proposed by Aurbach and Zaban [58], implements a layered SEI where inorganic decomposition products form the inner layers and organic products form the outer layers. The second model, proposed by Peled et al. [59], proposes a mosaic-type structure where SEI species are segregated into grains and where Li-ion transport is mainly along the grain boundaries. Similar to the Aurbach-Zaban model, the Peled model assumes that the inner SEI species are more inorganic and the outer microphases are more organic. Notably both layered and mosaic structures have been experimentally observed on Li anodes [25].

Despite the general acceptance of the Aurbach-Zaban and Peled models, such layered or mosaic-like structures are not captured in most continuum-level models. Instead, simpler reaction mechanisms and SEI composition (typically of a single SEI species) are proposed [60–66]. These chemically simple SEI models follow a diffusion-limited growth dynamic where the SEI grows with a square-root-of-time dependency. The change in SEI growth rate is attributed to surface film resistance growth and associated loss of lithium inventory. Chemically simple reduced-order models have significant utility in battery lifetime models [67], but because they sacrifice specificity in the SEI composition, they are less useful in SEI engineering.

Though most continuum-level SEI models have used reduced reaction mechanisms, a small number of more chemically complex models have been proposed [9, 61, 68–70]. Since the present manuscript focuses on a chemically complex continuum-level model, it is worthwhile to compare and contrast these previous approaches with the present approach.

Christensen and Newman [61] and Colclasure et al. [9] implemented SEI growth models on a graphite particle. Both of these models capture EC decomposition to Li_2CO_3 and C_2H_4 gas and use a moving boundary reformulation to capture SEI growth dynamics. To capture SEI species transport, both models implement dilute-solution theory and consider mobile species (e.g., Li-ions and electrons) supported by a lattice-like SEI. In either model, the chemical complexity of the electrolyte reduction and other reactive pathways are relegated to the the SEI surface sites and the bulk-phase SEI. The primary observation from the Christensen and Newman model is that the SEI growth rate depends on the electronic conductivity of the film at open-circuit conditions. Colclasure et al. [9] simulated both open-circuit voltage conditions and charge/discharge cycling. They found that the higher electrode state-of-charge promoted increased concentrations of electrons and Li-ions in the SEI. These higher concentrations promoted increased SEI growth that is limited by electron diffusion.

Single et al. [69] proposed a SEI model with global pathways from EC and dimethyl carbonate (DMC) to form lithium methyl carbonate (LMC), LEDC, Li_2CO_3, and lithium oxide (Li_2O). Unlike Christensen and Newman, Single proposed a porous SEI allowing electrolyte percolation. Additionally, instead of reformulating to a moving boundary domain, Single implements a self-consistent bulk velocity term to account for SEI growth. In their model, a total of two global reactions are proposed to reduce Li-coordinated EC and DMC to SEI-phase LEDC and LMC, respectively. A solid-phase conversion reaction is also proposed to convert LEDC to lithium oxide (Li_2O), which resulted in a dual-layer SEI. Single et al. [69] do not consider Li-ion transport in the SEI and instead assume that the electronic current can be treated according to Ohm's law.

Finally, Röder et al. [68] have proposed the potentially most advanced continuum-level modeling framework for battery SEI formation to date, albeit with arbitrary SEI species (labeled SEI_1, SEI_2, and SEI_3). In their framework, kMC models and continuum-level models are coupled together to predict SEI formation. In their kMC instance, SEI-species clustering and layering is observed due to assumed preferential binding energies and repulsive bonds. This clustering is consistent with the Peled model [59]. However, the Röder model assumes that all of the reactions are deposition-like reactions or solid-phase conversion reactions, ignoring the important role that electrolyte-phase reactions can play

Table 1: Chemical complexity of literature-reported continuum-level models.

Ref.	Electrode/SEI hetero. rxns	SEI homo. rxns	SEI species	SEI/electrolyte hetero. rxns	Interface species	Electrolyte homo. rxns	Electrolyte species
Present manuscript	1	0	**9**	**22**	–	**149**	**78**
Christensen & Newman [61]	3	0	4	8	6	–	4
Colclausure et al. [9]	3	1	6	8	6	–	4
Single et al. [69]	1	1	5	2	–	0	4
Röder et al. [68]	1	0	5	20	6	0	6
Korff et al. [70]	3*	–	–	–	–	5	9
Uppaluri et al. [60]	1	0	3	1	–	–	4

"–" indicates that the domain is not simulated. * Korff et al. [70] do not simulate a SEI, but rather an electrode/electrolyte interface. Their study is included because they simulate complex electrolyte homogeneous reactions.

on SEI formation. It is challenging to connect the Röder model with atomistic-scale models, as the thermochemistry and kinetics of surface and solid-phase reactions cannot be easily predicted by first-principles calculations. The Röder model was also unable to predict the square-root-of-time growth dynamics, which was well captured with either Ohm's law [69] or SEI Li-ion and electron transport [9, 61]. A more advanced kMC instance was recently published by the same group [71]. However, the updated kMC model has not yet been coupled to a continuum-level simulation.

The present manuscript is mainly aligned with the work from Christensen and Newman [61] and Colclasure et al. [9]. Similarities include using moving boundary domain reformulation and assuming that the SEI is a mixed conductor, with both Li-ion and electron transport captured in the SEI. The current manuscript greatly expands the chemical complexity of the electrolyte decomposition as compared to other continuum-level SEI models. Table 1 compares the number of reactions and species considered in other continuum-level models in the literature to the present manuscript. The present manuscript includes orders of magnitude more homogeneous electrolyte reactions and electrolyte species than other SEI models. The additional complexity is introduced because the present manuscript does not use global reactions, but rather uses an atomistically informed reaction mechanism derived from CRN analysis and DFT calculations. The present work represents a significant jump forward in SEI modeling by providing an upscaling scheme for modeling complex reaction networks, specifically emphasizing electrolyte-phase decomposition. The present single-particle framework is most appropriate for capturing the layered structure proposed by Aurbach and Zaban [58].

2. Methodology

Figure 1 illustrates the continuum-level model domain. Three domains are illustrated: the Si particle, the SEI, and the electrolyte. To demonstrate SEI growth dynamics, Si alloying physics are not captured [20]. The model is primarily concerned with SEI and electrolyte dynamics at a given voltage-hold (similar to Christensen and Newman's modeling at open-circuit potential [61]). As illustrated, the SEI is assumed to form a lattice structure with mobile Li-ion and electron species interstitial. At the SEI/electrolyte interface, heterogeneous reactions including reduction and deposition/dissolution are simulated. In the electrolyte, species migration, diffusion, and production are simulated. The reaction mechanism primarily includes homogeneous reactions in the electrolyte-phase. The model internal variables are species concentrations $[X_k]$, electrostatic potential Φ, and SEI thickness δ.

2.1. Species conservation

Species conservation can be expressed generally for any species k as

$$\frac{\partial [X_k]}{\partial t} = -\nabla \cdot \mathbf{J}_k + \dot{\omega}_k, \qquad (1)$$

where $\mathbf{J}_k$ is the species flux, and $\dot{\omega}_k$ is the volumetric species production rate. The volumetric production rate is discussed in Section 3. The species flux $\mathbf{J}_k$ can either be described using concentrated-solution or dilute-solution theory [72]. In dilute-solution theory, species transport results from the sum of diffusion, migration, and convection effects. The flux of species k using dilute-solution theory can be expressed mathematically as

$$\mathbf{J}_k = -D_k \nabla [X_k] - D_k \frac{z_k F}{RT} [X_k] \nabla \Phi + [X_k] \mathbf{v}, \quad (2)$$

where D_k is the species diffusion coefficient, z_k is the species charge, F is Faraday's constant, R is the gas constant, Φ is the potential, and $\mathbf{v}$ is the bulk velocity. The bulk velocity term is important because the SEI can expand/contract significantly during a simulation, which in-turn induces a bulk flow [69]. The bulk velocity due to SEI growth is handled intrinsically in the dynamic SEI-growth reference frame (Section 2.5) [73].
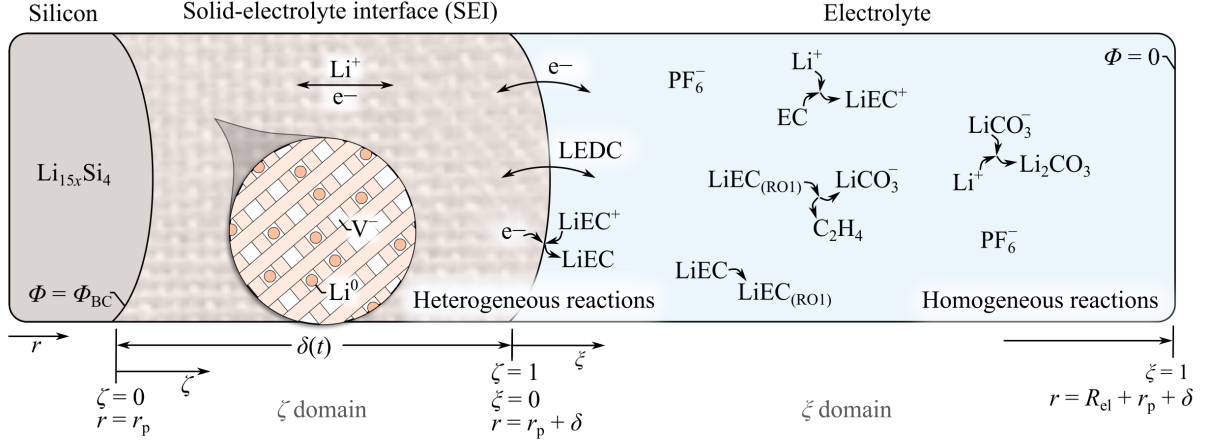
4

Figure 1: Model domain with representative physics, electrochemical/chemical reactions, independent coordinates, and select boundary conditions.

2.2. Electroneutrality

The local electrostatic potential Φ can either be resolved by assuming conservation of charge or by assuming electroneutrality. Conservation of charge is expressed mathematically as

$$\nabla \cdot \mathbf{i} + F \sum_k z_k \dot{\omega}_k = 0, \qquad (3)$$

$$\mathbf{i} = F \sum_k z_k \mathbf{J}_k, \qquad (4)$$

where $\mathbf{i}$ is the current density. Alternatively, the electrostatic potential Φ can be solved by assuming strict electroneutrality, which can be expressed as

$$F \sum_k z_k [X_k] = 0. \qquad (5)$$

When developing the model, both approaches in their native forms were fairly unstable and would result in either solver divergence or inability to take the first time-step. Ultimately, it was found that differentiating the strict electroneutrality equation (Eq. 5) in time to be

$$\sum_k z_k \frac{\partial [X_k]}{\partial t} = 0, \qquad (6)$$

resulted in the most stable governing equation to resolve potential. Importantly, "differentiating the constraint" is a viable approach if the initial species concentrations satisfy electroneutrality (Eq. 5) [74].

2.3. SEI lattice-site conservation

For the present modeling approach, the SEI is treated as a lattice structure similar to Colclasure et al. [9]. In this lattice structure, there are three kinds of species. First, there are species that form the SEI structure (e.g., LEDC or LiF). Second, there are species that occupy the lattice sites of this SEI structure (i.e., Li^0_{SEI}, V^-_{SEI}). Finally, there are interstitial species that are assumed to be mobile in the SEI (i.e., Li^+_{SEI}, e^-_{SEI}).

In the lattice structure, the lattice site concentration is assumed to be constant [72]. Lattice-site conservation can be expressed mathematically as

$$[Li^0_{SEI}] + [V^-_{SEI}] = C, \qquad (7)$$

where C is the constant total lattice-site concentration. Differentiating this lattice-constraint equation in time to improve numerical stability results in

$$\frac{\partial \left[Li^0_{SEI} \right]}{\partial t} + \frac{\partial \left[V^-_{SEI} \right]}{\partial t} = 0. \qquad (8)$$

Importantly, differentiating this constraint equation requires that the initial concentrations satisfy Eq. 7.

Noting that there is already a governing equation for conservation of species (Eq. 1), lattice conservation (Eq. 8) adds another, which over-defines the system. Meaning, for N species in the SEI there are $N + 1$ governing equations for these species. Thus, lattice-site conservation must replace a governing equation for one of the lattice-site species. The choice of which lattice species conservation equation is replaced by the lattice-site conservation is arbitrary. For the current implementation, the Li^0_{SEI} species conservation (Eq. 1) is replaced with the lattice-site conservation equation (Eq. 8).

2.4. SEI growth rate

During the simulation, the SEI is able to grow/shrink due to deposition/dissolution reactions at the

5

SEI/electrolyte interface. The SEI thickness δ is defined to spatially vary based on

$$\frac{\partial \delta}{\partial t} = \sum_{k,\text{struct}} \frac{W_k}{\rho_k} \dot{s}_k, \qquad (9)$$

where W_k is the species molecular weight, ρ_k is the species density, $\dot{s}_k$ is the species net surface production rate, and the summation is over SEI species that form the SEI structure (e.g., LEDC). This is the same approach as taken by Colclasure et al. [9]. This formulation assumes that the SEI thickness only changes due to interface deposition/dissolution reactions.

2.5. Moving boundary reformulation

To handle the dynamic SEI thickness changes, the model domain is transformed from a spatial mesh to a mesh that dynamically stretches/shrinks to changes in SEI thickness. In the present model, the SEI domain is transformed from the r-t domain to a ζ-τ domain, and the electrolyte domain is transformed from the r-t to a ξ-τ domain. (Note that ζ and ξ look similar, but are different symbols representing the spatially independent variable in the SEI and electrolyte domain, respectively). The new independent spatial variable ζ starts at the Si particle surface and is unity at the SEI/electrolyte interface (cf., Fig. 1). The independent variable ζ can be expressed mathematically as

$$\zeta = \frac{r - r_\text{p}}{\delta}, \qquad (10)$$

where r is the independent radial variable and r_p is the Si particle radius. The electrolyte independent spatial variable ξ starts at the SEI/electrolyte interface and is unity at a set radial distance from the Si particle surface R_el (cf., Fig. 1). The independent variable ξ can be expressed mathematically as

$$\xi = \frac{r - r_\text{p} - \delta}{R_\text{el} - r_\text{p} - \delta}. \qquad (11)$$

Note that R_el and r_p are assumed to be time invariant. From these definitions, the respective derivatives of ζ and ξ are

$$\left(\frac{\partial \zeta}{\partial r}\right)_t = \frac{1}{\delta}, \quad \left(\frac{\partial \zeta}{\partial t}\right)_r = \frac{-\zeta}{\delta} \frac{\partial \delta}{\partial t}, \qquad (12)$$

and

$$\left(\frac{\partial \xi}{\partial r}\right)_t = \frac{1}{R_\text{el} - r_\text{p} - \delta}, \quad \left(\frac{\partial \xi}{\partial t}\right)_r = \frac{\xi - 1}{R_\text{el} - r_\text{p} - \delta} \frac{\partial \delta}{\partial t}. \qquad (13)$$

A coordinate transformation is used to solve governing equations on the fixed mesh [61, 75, 76]. These transformation of variables can be complicated and prone to errors. So, the transformation is explained here in detail. A coordinate transformation can be expressed generally as [75]

$$A(r, t) = A\big(\zeta(r, t), \tau(r, t)\big), \qquad (14)$$

$$\left(\frac{\partial A}{\partial r}\right)_t = \left(\frac{\partial \zeta}{\partial r}\right)_t \left(\frac{\partial A}{\partial \zeta}\right)_\tau + \left(\frac{\partial \tau}{\partial r}\right)_t \left(\frac{\partial A}{\partial \tau}\right)_\zeta, \qquad (15)$$

$$\left(\frac{\partial A}{\partial t}\right)_r = \left(\frac{\partial \zeta}{\partial t}\right)_r \left(\frac{\partial A}{\partial \zeta}\right)_\tau + \left(\frac{\partial \tau}{\partial t}\right)_r \left(\frac{\partial A}{\partial \tau}\right)_\zeta, \qquad (16)$$

where A is some dependent variable. For these particular transformations $t = \tau$. The transformation of variables for the SEI domain can be expressed as

$$\left(\frac{\partial A}{\partial r}\right)_t = \frac{1}{\delta} \left(\frac{\partial A}{\partial \zeta}\right)_\tau, \qquad (17)$$

$$\left(\frac{\partial A}{\partial t}\right)_r = \frac{-\zeta}{\delta} \frac{\partial \delta}{\partial \tau} \left(\frac{\partial A}{\partial \zeta}\right)_\tau + \left(\frac{\partial A}{\partial \tau}\right)_\zeta. \qquad (18)$$

This transformation is commonly referred to as the Landau transformation [60, 73, 76]. In the electrolyte domain, the transformation of variables can be expressed as

$$\left(\frac{\partial A}{\partial r}\right)_t = \frac{1}{R_\text{el} - r_\text{p} - \delta} \left(\frac{\partial A}{\partial \xi}\right)_\tau, \qquad (19)$$

$$\left(\frac{\partial A}{\partial t}\right)_r = \frac{\xi - 1}{R_\text{el} - r_\text{p} - \delta} \frac{\partial \delta}{\partial \tau} \left(\frac{\partial A}{\partial \xi}\right)_\tau + \left(\frac{\partial A}{\partial \tau}\right)_\xi. \qquad (20)$$

In the original spatial domain, species conservation can be expressed as

$$\frac{\partial [X_k]}{\partial t} = \nabla \cdot \left(D_k \nabla [X_k] + D_k \frac{z_k F}{RT} [X_k] \nabla \Phi\right) + \dot{\omega}_k, \qquad (21)$$

Using the Landau transformation on SEI species conservation (Eq. 21), the transformed SEI species conservation of species is expressed as

$$\frac{\partial [X_k]}{\partial \tau} + \left(\frac{-\zeta}{\delta} \frac{\partial [X_k]}{\partial \zeta}\right) \frac{\partial \delta}{\partial \tau} =$$
$$\frac{1}{\delta^2 r^2} \frac{\partial}{\partial \zeta} \left(r^2 D_k \frac{\partial [X_k]}{\partial \zeta} + r^2 D_k \frac{z_k F [X_k]}{RT} \frac{\partial \Phi}{\partial \zeta}\right) + \dot{\omega}_k. \qquad (22)$$

Previous SEI model manuscripts have also used the Landau transformation to account for the moving boundary in the SEI domain [9, 60, 61]. Similarly, the

6

transformed electrolyte species conservation can be expressed as

$$\frac{\partial [X_k]}{\partial \tau} + \left(\frac{\xi - 1}{R_{\text{el}} - r_{\text{p}} - \delta} \frac{\partial [X_k]}{\partial \xi} \right) \frac{\partial \delta}{\partial \tau} =$$
$$\frac{1}{\left(R_{\text{el}} - r_{\text{p}} - \delta \right)^2 r^2} \frac{\partial}{\partial \xi} \left(r^2 D_k \frac{\partial [X_k]}{\partial \xi} + r^2 D_k \frac{z_k F [X_k]}{RT} \frac{\partial \Phi}{\partial \xi} \right)$$
$$+ \dot{\omega}_k. \tag{23}$$

In the fixed ζ-transformed domain, conservation of lattice sites can be differentiated in transformed time to be

$$\frac{\partial \left[\text{Li}^0_{\text{SEI}} \right]}{\partial \tau} + \frac{\partial \left[\text{V}^-_{\text{SEI}} \right]}{\partial \tau} \qquad (24)$$
$$- \frac{\zeta}{\delta} \frac{\partial}{\partial \zeta} \left(\left[\text{Li}^0_{\text{SEI}} \right] + \left[\text{V}^-_{\text{SEI}} \right] \right) \frac{\partial \delta}{\partial \tau} = 0.$$

Noting that the $\partial \delta / \partial \tau$ term contains lattice site conservation (i.e., the spatial derivative of a constant is zero) results in

$$\frac{\partial \left[\text{Li}^0_{\text{SEI}} \right]}{\partial \tau} + \frac{\partial \left[\text{V}^-_{\text{SEI}} \right]}{\partial \tau} = 0. \tag{25}$$

Similarly, the differentiated electroneutrality constraint (Eq. 6) can be expressed as

$$\sum_k z_k \frac{\partial [X_k]}{\partial \tau} = 0. \tag{26}$$

Notably, Eq. 26 is the same governing equation for potential Φ in the SEI domain using the ζ-τ transformation as it is in the electrolyte domain using the ξ-τ transformation. The coupled set of partial differential equations is reduced to a set of ordinary differential equations using the method of lines [75], and is subsequently solved in MATLAB using the ode15s solver with a variable-dependent Mass matrix.

2.6. Initial conditions

The initial SEI is assumed to start as a 1 nm thick layer of LiF before the voltage-hold, which is consistent with previous continuum-level model approaches [9, 61, 69]. This initial SEI layer is required in the continuum-level model so that all phases are initiated at the beginning of the simulation. In other words, the continuum-level model does not allow for instantaneous phase creation, rather only phase growth/shrinkage. The potential equation is specified to be uniform in each domain propagating from the domain-specific boundary condition. For example, the SEI is assumed to be at a potential of $\Phi_{\text{SEI}}(\zeta, t = 0) = \Phi_{\text{SEI}}|_{\zeta=0}$ and the electrolyte

potential is assumed to be $\Phi_{\text{el}}(\zeta, t = 0) = \Phi_{\text{el}}|_{\zeta_{\text{max}}}$. The potential governing equation is essentially an algebraic constraint equation that implicitly depends on potential (cf., Eq. 26), so a reasonable guess is needed to initiate the solver.

The initial species concentrations are sometimes difficult to determine in a stable manner for the SEI model. For example, if the starting concentrations of Gen2F electrolyte (1.2 M Li salt in 3:7 wt/wt EC:EMC with 3 wt.% FEC) are used as starting initial concentrations, the solver is extremely slow and may not converge to take the initial time step. This instability is mainly because uncoordinated Li-ions in solution are very unstable and quickly react to form complexes such as Li$^+$EC, Li$^+$EMC, and Li$^+$FEC in solution. In other words, it is unphysical to start the SEI model with significant concentrations of uncoordinated Li-ions. However, knowing the starting concentration of coordinated complexes a priori is non-trivial. Thus, before initiating the SEI reaction model, a simple perfectly stirred reactor model is used to determine the relative concentrations of Li-coordinated complexes in the electrolyte. The perfectly stirred reactor model solves

$$\frac{\partial [X_k]}{\partial t} = \dot{\omega}_k. \tag{27}$$

Note that no reduction reactions are simulated in the perfectly stirred reactor model (i.e., $\dot{s}_k = 0$). The perfectly stirred reactor model simply provides the equilibrium concentrations of Li-coordinated complexes in solution. The initial electrolyte species concentrations for the perfectly stirred reactor are specified in Table 2. Once the perfectly stirred reactor model reaches a steady-state, these steady-state concentrations are used to initialize the electrolyte species concentrations in the SEI continuum-level model. In the SEI continuum-level model, the species concentrations are assumed to be uniform spatially within each of their respective domains.

The first few time steps can be difficult for the stiff solver in the SEI continuum-level model to converge. To resolve this issue, the surface reaction net rates of progress $\dot{s}_k$ and homogeneous net rates of progress $\dot{\omega}_k$ are smoothly activated from initial condition using

$$\Gamma = \left(1 - 10^{-20} \right) \tanh \left(0.05 \, t \right) + 10^{-20}, \tag{28}$$

where Γ modulates the net rates of progress, and t is time in seconds. This essentially "turns on" the surface reactions in a smooth manner in the first 100 s of simulation. A similar numerical trick was employed in Colclasure et al. [9].

Table 2: Initial conditions for the perfectly stirred reactor

	Parameter	Description	Value	Unit
Si particle				
	r_p	Si particle radius	75	nm
SEI interphase				
	$\delta\|_{t=0}$	Initial SEI thickness	1	nm
	$[V^-_{SEI}]_{t=0}$	Initial vacancy concentration	5.2	mol m^{-3}
	$[Li_{SEI}]_{t=0}$	Initial interstitial lithium concentration	5.2	mol m^{-3}
	$[Li^+_{SEI}]_{t=0}$	Initial lithium-ion concentration$^\circ$	10.4	mol m^{-3}
	$[e^-_{SEI}]_{t=0}$	Initial electron concentration$^\circ$	5.2	mol m^{-3}
	$[LiF_{SEI}]_{t=0}$	Initial LiF concentration	101.57	kmol m^{-3}
Electrolyte*				
	$[EC_{el}]_{t=0}$	Initial EC concentration	3.359	kmol m^{-3}
	$[FEC_{el}]_{t=0}$	Initial FEC concentration	0.293	kmol m^{-3}
	$[EMC_{el}]_{t=0}$	Initial EMC concentration	6.510	kmol m^{-3}
	$[PF^-_{6\,el}]_{t=0}$	Initial PF$_6^+$ concentration	1.286	kmol m^{-3}
	$[Li^+_{\,el}]_{t=0}$	Initial lithium-ion concentration	1.286	kmol m^{-3}
	R_{el}	Maximum domain radius	2	μm

* These concentrations are used to initialize the perfectly stirred reactor model.
The concentrations correspond to a 1.2 M LiPF$_6$ salt in Gen2 electrolyte (3:7 wt% EC:EMC) with 3% FEC – Referred to as Gen2F.
The SEI concentrations are near that of Colclasure et al. [9]

2.7. Boundary conditions

At the far edge of the electrolyte boundary (see right-side of Fig. 1, $\xi = 1$), the electrolyte species concentration is assumed to have a no-flux condition for all non-charged species. For charged species (e.g., Li$^+$EC$_{el}$, PF$_{6\,el}^-$, Li$^+_{\,el}$) at the electrolyte external boundary, the boundary condition is a constant concentration. A no-flux condition cannot be specified for charged species since a net current is developed from side reactions. Thus, a no-flux condition for charged species at the external boundary would violate conservation of current. The electrolyte potential is set to reference at the far boundary ($\Phi_{el}\|_{\zeta=\zeta_{max}} = 0$).

At the SEI/electrolyte boundary, in radial coordinates, species flux is due to both surface reactions and the moving boundary. However, in the transformed coordinate frame, the convective flux due to the moving boundary is handled separately. This means that the surface flux at the SEI/electrolyte interface is due to surface reactions only, which in ζ space, can be expressed as

$$\left(\mathbf{J}_k \cdot \mathbf{n} - [X_k]\frac{\partial\delta}{\partial\tau}\right)_{\zeta=1} = \left.-\Gamma\dot{s}_k\right|_{\zeta=1}, \qquad (29)$$

where $\mathbf{n}$ is the unit normal vector, and $\mathbf{J}_k$ is the species flux in the moving-boundary frame. This same boundary condition is imposed for the electrolyte domain at the $\xi = 0$ interface.

At the anode/SEI boundary (left-side of Fig. 1), the electron concentration is set such that the following reaction is in equilibrium

$$e^-_{SEI} \leftrightharpoons e^-_{Si}. \qquad (30)$$

This approach is the same as other continuum-level models [9, 61]. Assuming that the electron from the Si

phase is defined by the potential, the electron concentration in the SEI at the Si interface is

$$\left[e^-_{SEI}\right] = \left[e^-_{SEI}\right]_0 \exp\left(\frac{-\mu^\circ_{e^-_{SEI}}}{RT}\right), \qquad (31)$$

where $\left[e^-_{SEI}\right]_0$ is the standard-state electron concentration. Additionally, the Si is assumed to be at an equilibrium lithiated state. This is equivalent to a no-flux condition for Li species at the anode/SEI interface. Finally, the potential $\Phi_{SEI}\|_{\zeta=0}$ is set to the prescribed voltage-hold value.

2.8. Species transport

The model implements dilute-solution theory to predict species transport. This is an important simplification since concentrated-solution effects are assumed to be significant in battery electrolytes [77]. However, the number of unknown diffusion parameters significantly increases if off-diagonal Onsager effects are considered (i.e., N transport properties in dilute solution theory is instead NxN transport properties in concentrated solution theory) [72]. This is a challenge when considering a general reaction network where a significant number of electrolyte species are generated[1]. Thus, a general theory is required that can approximate electrolyte species transport similar to the kinetic theory available for gas-phase species transport [72, 78–81].

Species diffusion also relates to solvation shell effects and whether the ion transport is primarily due

---

[1]It is possible to reduce the number of required transport properties by only considering properties for long-lived, non-intermediate species.

to shuttling/vehicular-transport or metal-hopping [82]. The primary transport mode in battery electrolytes has been studied using first-principles MD. These studies indicate that Li-ions in EC and DMC electrolytes can hop between solvation cages, while EC/EMC-containing electrolytes have a primarily vehicular transport mechanism [82, 83]. These solvation-shell effects and associated transport also depend on the salt concentration, which can ultimately influence the measured solid-phase SEI composition [8, 23, 38]. At the continuum-level, these effects can be captured by simulating reversible salt-coordination/metal-hopping reactions (and associated thermodynamics) and solvated-structure transport properties. In the present study, Li-ions can coordinate to EC, EMC, and FEC, and electrolyte species diffusion is assumed to act as a dilute solution with metal-hopping reactions captured (see Table S4).

In the electrolyte, species diffusion coefficients are chosen such that the electrolyte conductivity is ≈ 10 mS cm^{-1} and the transport number is 0.4, which is reasonable for this electrolyte formulation [84, 85]. To achieve these bulk phase transport properties, as a first approximation, all electrolyte species (other than PF_6^-) are assumed to have the same diffusion coefficient of $D_{k,\text{el}} = 9\text{E}-11$ [m^2 s^{-1}]. The PF_6^- species is assumed to have a diffusion coefficient of 2.25E-10 m^2 s^{-1}, which results in a transport number of 0.4. Note that in dilute solution theory, the ionic conductivity σ is related to the species self-diffusion coefficients as [72]

$$\sigma = \frac{F^2}{RT} \sum_k z_k^2 D_k \left[X_k \right]. \tag{32}$$

The simulation results are somewhat sensitive to the assumed self-diffusion coefficients. Mainly, if the diffusion coefficient is too high, then intermediate species can leave the reducing SEI surface and a build-up of intermediate products is observed in the bulk electrolyte phase. The model would be improved by implementing a more general transport theory to relax these transport assumptions [78–80].

In the SEI, the most mobile species (i.e., Li^+_{SEI}, V^-_{SEI}, and Li_{SEI}) are assigned diffusion coefficients of 2E-14 m^2 s^{-1}, which are taken from literature [9]. The structural species (i.e., $Li_2CO_{3\text{SEI}}$, $LEDC_{\text{SEI}}$, LiF_{SEI}, LMC_{SEI}, and LEC_{SEI} (lithium ethyl carbonate)) are assigned a very slow diffusion coefficient of 3E-24 m^2 s^{-1}. In the model, the only "free parameter" is the diffusion coefficient of the electron in the SEI phase. The electron diffusion coefficient is assumed to depend on the SEI potential and is calibrated such that the predicted leak-age current is on the same scale as the measured leakage current. All species transport properties are documented in Table 3.

3. Atomistically informed reaction mechanism

The preceding discussion has focused on formulating the SEI/electrolyte continuum-level model in general terms. That is, the model is meant to accept any given reaction mechanism developed at the atomistic scale and quickly predict SEI dynamics. The reaction mechanism – which describes the relevant phases (i.e., SEI and electrolyte), species in each phase, species thermodynamics and properties, reaction pathways, and reaction rates – is introduced to the continuum-level model via the open source Cantera package [72, 86, 87].

The reaction mechanism described here is obtained from atomistic analysis of elementary reaction pathways obtained via a combination of previous CRN analysis and by-hand searches. The mechanism includes pathways to the solid SEI products LEDC, Li_2CO_3, LMC, LEC, and LiF, as well as the gaseous byproducts CO, CO_2, CH_4, C_2H_2, C_2H_4, C_2H_6, C_3H_6, C_3H_8, and C_4H_8. Reaction thermodynamics and kinetics for homogeneous electrolyte reactions and heterogeneous reduction reactions (involving an electron from the SEI phase and a reducing species in the electrolyte phase) are obtained using DFT combined with transition state theory (for homogeneous electrolyte reactions) and Marcus theory (for reduction reactions).

While DFT and CRNs are able to provide considerable detail regarding the electrolyte phase, certain phenomena are not well captured by these methods alone. To account for the changing local solvation environments of Li^+, metal hopping reactions of the type $Li-A + B \rightleftharpoons A + Li-B$ are included, with kinetics obtained via a combination of DFT-calculated thermochemistry and Li^+ residence times obtained from classical MD simulations [51, 88]. Reactions for the precipitation of solid products to form the SEI and the dissolution of SEI species are assumed (see Table S2). Specifically, in the current model, five species that form in the electrolyte phase are assumed to favorably deposit to form the SEI: LEDC, Li_2CO_3, LMC, LEC, and LiF.

3.1. Species thermodynamics

Thermochemical parameters for species in the electrolyte phase are calculated in the Q-Chem electronic structure code [89] using the ωB97X-V density functional [90] and def2-TZVPPD basis set [91]. Explicit solvent shells are not considered, primarily due to the

computational cost of solvent cluster calculations. Instead, solvent effects are captured implicitly using the solvent model with density (SMD) [92], with parameters appropriate for an electrolyte comprised of EC and EMC. For most species, these thermochemical parameters were previously published in the Lithium-Ion Battery Electrolyte (LIBE) dataset [93]. All species properties are assumed to follow a constant-volume equation of state for an ideal-condensed phase.

Due to the complex, heterogeneous structure and composition of the SEI, it is far more difficult to calculate the thermochemistry of species in the SEI phase. In the present model framework, the only SEI species that participate in reactions are e_{SEI}^- species and deposition products that form in the electrolyte phase. The thermodynamics of the electron species are specified such that the electrochemical reduction reactions with the electrolyte species occur nominally at the voltages reported in literature (cf., Table S2) [9, 69]. The species thermodynamics of known deposition products (e.g., LiF_{SEI}, $LEDC_{SEI}$, and $Li_2CO_{3,SEI}$) are chosen such that the net production of deposited species is favorable. By assuming that species deposition is thermodynamically favorable, the SEI only grows. Thus, SEI "breathing" [11, 94] is not currently captured in the model.

Ideally, species participating in deposition/dissolution reactions to form the SEI would have thermodynamics that are informed by measured solubility [15, 95, 96] or atomistic modeling [97, 98]. Table S1 documents common SEI species identified in the literature with notes associated with their solubility and observed deposition locations. Of note, there can be significant differences in experimental observations on relative species solubilities (see Table S1). In principle, species solubility thermodynamics can be computed by accounting for the heat of sublimation and heat of solution to obtain the heat of dissolution [97, 99]. However, these computations are highly sensitive to the local electrolyte environment and SEI surface sites, making them challenging to employ when the exact structure of the SEI and electrode surface are unknown.

3.2. Reactions

Elementary reaction pathways were obtained using the AutoTS workflow [100], which leverages the Jaguar electronic structure code [101]. Transition states were initially optimized using the ωB97X-D density functional [102] with the def2-SVPD(-f) basis set [91] and the polarizable continuum model (PCM) implicit solvent environment [103] using the parameters for water. Each transition state was confirmed to be connected to the expected reaction endpoints by perturbing

the transition state along the transition normal mode in the forwards and reverse direction and using a geometry optimization with the same ωB97X-D/def2-SVPD(-f)/PCM(water) level of theory. For each reaction, the electronic energies of the optimized transition state and reaction endpoints were corrected with Q-Chem using the ωB97X-V/def2-TZVPPD/SMD(EC/EMC) level of theory, making the calculations of energy barriers consistent with the thermochemical calculations discussed above. We note that the thermodynamics and kinetics of some reactions, particularly for EC decomposition reactions, were reported previously by Spotte-Smith, Kam, et al. [50]. In the current mechanism, slow pathways ($\Delta G^{\ddagger} \gtrsim 0.8$ eV) are excluded, as these reactions are not expected to contribute significantly to the SEI formation and growth. At present, the decomposition of SEI species such as LEDC is also not included, though it is expected that such decomposition routes are possible and even important in understanding long-term SEI behavior. For example, Yoon et al. [104] used thermogravimetric analysis, complemented by IR and XPS analysis of cycled Si anodes, to suggest a thermal decomposition mechanism of $LEDC_{SEI} \rightarrow Li_2CO_{3SEI} + C_2H_4 + CO_2 +$ "O" resulting from long-term cycling.

Figure 2 illustrates the reactions considered in the present continuum-level model [93]. These reactions represent facile pathways for EC, EMC, and FEC decomposition to known SEI components and gaseous byproducts. Most reaction pathways involve only homogeneous reactions in the electrolyte phase and heterogeneous reduction reactions involving an electron from the SEI phase and a species from the electrolyte phase that can be reduced. The other heterogeneous reactions considered in the system are deposition/dissolution reaction that increase the SEI thickness. The forward rate constants for deposition reactions are assumed to be relatively fast, which assumes that SEI-depositing species tends to quickly deposit once formed in the electrolyte phase near the SEI interface. Table S2 documents the reversible heterogeneous reactions with their forward rate constants, reorganization energy, and equilibrium potentials.

Figure 2: Reaction mechanism considered in the present manuscript. Reactions include predominant decomposition mechanisms for EC, EMC, DMC, DEC, VC, PC, BC, and FEC. Species are labelled as SX, where X is the species number in Table S2. Reactions and rates are documented in Table S3 and Table S4. Heterogeneous reactions are documented in Table S2.

11
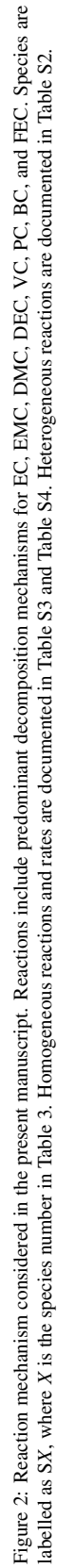
In general, these reactions are elementary, meaning that one transition-state links the reactants and the products. In pathways where intermediates could be formed and consumed with a single rate-limiting step, if those intermediates were not involved in any other reactions, we combined several steps, treating the barrier of the rate-limiting step as the overall barrier for the reaction. This reduced the number of species that need to be tracked in the model with minimal effect on the overall system dynamics. As discussed previously [50], the energy barriers for cyclic carbonate ring-opening reactions at the waist bond (e.g. $S_{41} \longrightarrow S_{43}$ in Fig. 2) are highly sensitive to the chosen computational method, and in particular, we believe that the ωB97X-V/def2-TZVPPD/SMD(EC/EMC) may underestimate the rate of these reactions. As such, we have set the barriers $\Delta G^{\ddagger}$ for all of these reactions to 0.4 eV (where 0 eV is barrierless and 0.8 eV is a significantly high barrier).

As discussed in Section 2.8, metal-hopping reactions are included to account for changes in Li-ion solvation and coordination. MD simulations have found that typical Li$^+$ residence times are $\approx$5 ns [51], which imply an effective barrier for metal hopping of $\approx$0.26 eV. Here, we assume that 0.26 eV is the minimum barrier for all metal hopping reactions (Table S4).

For heterogeneous reduction reactions, the forward rate constants are determined using Marcus theory [105]. To compute the forward rate constant for electron transfer kinetics, several assumptions are required including reorganization energies, electron coupling and pre-factor estimation. The electron transfer rate can be expressed as

$$k_{ET} = \frac{\kappa_0 k_B T}{h} \exp(-\beta R) \exp\left(\frac{-1}{4k_B T} \frac{(\lambda + \Delta G)^2}{\lambda}\right), \quad (33)$$

where k_{ET} is the electron transfer forward rate in s^{-1}, κ_0 is the tunneling coefficient pre-factor (taken as unity), β is the sensitivity term (taken as 1 nm^{-1}), k_B is the Boltzmann constant, T is temperature, λ is the reorganization energy, h is Planck's constant, and ΔG is the reaction free energy (calculated using DFT). The reorganization energy is made up of an inner reorganization energy and an outer reorganization energy ($\lambda = \lambda_{inner} + \lambda_{outer}$). The inner reorganization energy λ_{inner} is computed using the four-point method of Nelsen [106] with DFT at the ωB97X-V/def2-TZVPPD/SMD(EC/EMC) level of theory. The outer reorganization energy λ_{outer}, which depends on the bulk electrolyte environment and is as a result difficult to predict, is specified as a constant of 0.8 eV in the present study.

The total surface reaction (in m s^{-1}), can be expressed

as

$$\kappa_{surf,ET} = \int_{R_{min}}^{\infty} k_{ET} \, dR$$
$$= \frac{\kappa_0 k_B T}{h} \int_{R_{min}}^{\infty} \exp(-\beta R) \exp\left(\frac{-1}{4k_B T} \frac{(\lambda + \Delta G)^2}{\lambda}\right) dR, \quad (34)$$

where R_{min} is the minimum distance to the electrode (taken to be $\approx$2Å). Assuming that the second exponential doesn't strongly change with radius R, the integral results in

$$\kappa_{surf,ET} \approx \frac{\kappa_0 k_B T \exp(-\beta R_{min})}{h\beta} \exp\left(\frac{-1}{4k_B T} \frac{(\lambda + \Delta G)^2}{\lambda}\right). \quad (35)$$

The electron-transfer forward rate coefficient is then

$$\kappa_{surf,ET} \approx \frac{k_{ET}|_{R=R_{min}}}{\beta}. \quad (36)$$

The electrolyte decomposition and SEI-forming products depend significantly on the 1) equilibrium concentrations of Li-ion coordinated complexes, 2) thermodynamics of the reactants and products, and 3) reaction energy barriers. The perfectly stirred reactor (Section 2.6) is used to determine the equilibrium concentrations between Li$^+$, LiEC$^+$, LiEMC$^+$, and LiFEC$^+$ in solution before introducing a reductive surface. Using the species thermodynamics (Table 3) and metal-hopping reactions (Table S4), the equilibrium concentrations before starting the SEI model are determined to be 2.95E-19 (Li$^+$), 0.630 (LiEC$^+$), 0.544 (LiEMC$^+$), and 0.030 (LiFEC$^+$) kmol m^{-3}. These concentrations can also be expressed relatively as Li-ion coordinated species versus uncoordinated species, i.e. 0.143 ([LiEC$^+$]/[EC]), 0.11 ([LiEMC$^+$]/[EMC]), and 0.124 ([LiFEC$^+$]/[FEC]). Note that, in a real electrolyte, Li$^+$ is typically coordinated by multiple (4-5) solvents or anions [51]. However, here it is assumed that Li$^+$ is at any point coordinated only by one molecule to keep the number and types of species in the model tractable (i.e., so that the population of all possible solvation environments does not need to be tracked).

After determining the initial Li-coordinated equilibrium concentrations, the SEI model is used to simulate electrolyte reduction, and ultimately SEI formation. The electron reduction reactions are determined using Marcus theory and depend on the participating species thermodynamics (see ΔG in Eq. 33). For reduction reactions, it is convenient to determine the equilibrium potential E^{eq} from species thermodynamics (Table S2). The starting Li-coordinated complexes are predicted to

12

Table 3: Species thermodynamics and transport properties

	Species name	Chemical composition	Enthalpy, $h°$/(eV)	Entropy, $s°$/(eV K^{-1})	Molar volume, Ω_k/(cm^3 mol^{-1})	Diffusion coeff., D_k/(m^2 s^{-1})
SEI						
1	Li^+_{SEI}	Li:1, E:-1	–	–	–	2E−14*
2	V_{SEI}	E:-1	–	–	–	2E−14*
3	$Li_2CO_{3,SEI}$	Li:2, C:1, O:3	-7.5920E+3‡	3.1594E-3‡	36.95	3E-24∥
4	Li_2EDC_{SEI}	Li:2, C:4, H:4, O:6	-1.7344E+5‡	4.8434E-3‡	96.20	3E-24∥
5	e^-_{SEI}	E:-1	-1.3008E-1	3.4689E-3	–	D_{e^-}
6	Li_{SEI}	Li:1	–	–	–	2E−14*
7	LiF_{SEI}	Li:1, F:1	-3.0353E+3‡	2.0885E-3‡	5.20	3E-24∥
8	LEC_{SEI}	Li:1, C:3, H:4, O:3	-1.3008E+4‡	3.4027E-3‡	66.7*	3E-24∥
9	LMC_{SEI}	Li:1, C:2, H:3, O:3	-8.6722E+3‡	3.3421E-3‡	66.7*	3E-24∥
Electrolyte						
1	EC_{el}	C:3, H:4, O:3	-9.3165E+03	3.1102E-03	–	9E-11
2	FEC_{el}	C:3, F:1, H:3, O:3	-1.2017E+04	3.2817E-03	–	9E-11
3	EMC_{el}	C:4, H:8, O:3	-1.0417E+04	3.8132E-03	–	9E-11
4	PF^-_{6el}	P:1, F:6, E:1	–	–	–	2.25E-10
5	Li^+_{el}	Li:1, E:-1	-2.0106E+02	6.4222E-05	–	9E-11
6	$LiEC^+_{el}$	Li:1, C:3, H:4, O:3, E:-1	-9.5184E+03	3.5374E-03	–	9E-11
7	$LiFEC^+_{el}$	Li:1, C:3, F:1, H:3, O:3, E:-1	-1.2219E+04	3.6968E-03	–	9E-11
8	$LiEMC^+_{el}$	Li:1, C:4, H:8, O:3, E:-1	-1.0619E+04	4.2217E-03	–	9E-11
9	C_2H_{2el}	C:2, H:2	-2.1036E+03	2.1102E-03	–	9E-11
10	C_2H_{4el}	C:2, H:4	-2.1370E+03	2.3870E-03	–	9E-11
11	C_3H_{6el}	C:3, H:6	-3.2063E+03	2.7392E-03	–	9E-11
12	CO_{el}	C:1, O:1	-3.0833E+03	2.0464E-03	–	9E-11
13	CO_{2el}	C:1, O:2	-5.1318E+03	2.2130E-03	–	9E-11
14	CH_{4el}	C:1, H:4	-1.1011E+03	2.1431E-03	–	9E-11
15	C_2H_{6el}	C:2, H:6	-2.1702E+03	2.5169E-03	–	9E-11
16	C_3H_{8el}	C:3, H:8	-3.2393E+03	2.8450E-03	–	9E-11
17	C_4H_{8el}	C:4, H:8	-4.2754E+03	3.0768E-03	–	9E-11
18	$LiEMC_{el}$	Li:1, C:4, H:8, O:3	-1.0621E+04	4.1946E-03	–	9E-11
19	VC_{el}	C:3, H:2, O:3	-9.2835E+03	2.9838E-03	–	9E-11
20	$LiVC^+_{el}$	Li:1, C:3, H:2, O:3, E:-1	-9.4854E+03	3.4052E-03	–	9E-11
21	BC_{el}	C:5, H:8, O:3	-1.1454E+04	3.7358E-03	–	9E-11
22	$LiBC^+_{el}$	Li:1, C:5, H:8, O:3, E:-1	-1.1657E+04	4.1491E-03	–	9E-11
23	PC_{el}	C:4, H:6, O:3	-1.0385E+04	3.4140E-03	–	9E-11
24	$LiPC^+_{el}$	Li:1, C:4, H:6, O:3, E:-1	-1.0587E+04	3.8828E-03	–	9E-11
25	$FEC\_RO\_lessLiF_{el}$	C:3, H:3, O:3	-9.2979E+03	3.4727E-03	–	9E-11
26	$LiOCH_{3el}$	Li:1, C:1, H:3, O:1	-3.3374E+03	2.7658E-03	–	9E-11
27	$CH_3CH_2OCO_{el}$	C:3, H:5, O:2	-7.2835E+03	3.2997E-03	–	9E-11
28	$LiCH_3CH_2OCO^+_{el}$	Li:1, C:3, H:5, O:2, E:-1	-7.4853E+03	3.7337E-03	–	9E-11
29	CH_3OCO_{el}	C:2, H:3, O:2	-6.2142E+03	2.9686E-03	–	9E-11
30	$LiCH_3OCO^+_{el}$	Li:1, C:2, H:3, O:2, E:-1	-6.4160E+03	3.4506E-03	–	9E-11
31	DEC_{el}	C:5, H:10, O:3	-1.1487E+04	4.1494E-03	–	9E-11
32	$LiDEC^+_{el}$	Li:1, C:5, H:10, O:3, E:-1	-1.1689E+04	4.5519E-03	–	9E-11
33	DMC_{el}	C:3, H:6, O:3	-9.3485E+03	3.4912E-03	–	9E-11
34	$LiDMC^+_{el}$	Li:1, C:3, H:6, O:3, E:-1	-9.5505E+03	3.8882E-03	–	9E-11
35	FEC_lessH_{el}	C:3, F:1, H:2, O:3	-1.1999E+04	3.3007E-03	–	9E-11
36	$moec_{el}$	C:4, H:6, O:4	-2.8671E+05	9.0653E+01	–	9E-11
37	$eoec_{el}$	C:5, H:8, O:4	-3.1137E+05	9.7282E+01	–	9E-11
38	$methoxydioxolanone_{el}$	C:4, H:6, O:4	-2.8671E+05	8.3248E+01	–	9E-11
39	$ethoxydioxolanone_{el}$	C:5, H:8, O:4	-3.1138E+05	9.2486E+01	–	9E-11
40	EC_lessH_{el}	C:3, H:3, O:3	-9.2987E+03	3.1132E-03	–	0†
41	$LiEC_{el}$	Li:1, C:3, H:4, O:3	-9.5206E+03	3.4026E-03	–	0†
42	$LiEC^-_{el}$	Li:1, C:3, H:4, O:3, E:1	-9.5224E+03	3.4061E-03	–	0†
43	$LiEC\_RO_{el}$	Li:1, C:3, H:4, O:3	-9.5218E+03	3.7227E-03	–	0†
44	$LiEC\_RO^-_{el}$	Li:1, C:3, H:4, O:3, E:1	-9.5247E+03	3.6540E-03	–	0†
45	$LiEC\_RO\_shoulder_{el}$	Li:1, C:3, H:4, O:3	-9.5241E+03	3.5061E-03	–	0†
46	$LiVC_{el}$	Li:1, C:3, H:2, O:3	-9.4877E+03	3.3309E-03	–	0†
47	$LiVC\_RO_{el}$	Li:1, C:3, H:2, O:3	-9.4882E+03	3.5990E-03	–	0†
48	$LiVC\_RO^-_{el}$	Li:1, C:3, H:2, O:3, E:1	-9.4920E+03	3.5712E-03	–	0†
49	$LiFEC_{el}$	Li:1, C:3, F:1, H:3, O:3	-1.2221E+04	3.5876E-03	–	0†
50	$FEC\_RO\_lessLiF^-_{el}$	C:3, H:3, O:3, E:1	-9.3016E+03	3.3414E-03	–	0†
51	$LiDMC_{el}$	Li:1, C:3, H:6, O:3	-9.5525E+03	3.8865E-03	–	0†
52	$LiCO^-_{3el}$	Li:1, C:1, O:3	-7.3887E+03	2.9208E-03	–	0†
53	$LEDC_{el}$	Li:2, C:4, H:4, O:6	-1.6909E+04	4.8438E-03	–	0†
54	$LEDC\_lessLi^-_{el}$	Li:1, C:4, H:4, O:6, E:1	-1.6705E+04	4.5836E-03	–	0†
55	$Li(OCH_2)_{2el}^-$	Li:1, C:2, H:4, O:2, E:1	-6.4404E+03	3.0395E-03	–	0†
56	LMC_{el}	Li:1, C:2, H:3, O:3	-8.4705E+03	3.3420E-03	–	0†
57	$LiCO^+_{2el}$	Li:1, C:1, O:2, E:-1	-5.3332E+03	2.6167E-03	–	0†
58	Li_2CO_{3el}	Li:2, C:1, O:3	-7.5924E+03	3.1583E-03	–	0†
59	LiF_{el}	Li:1, F:1	-2.9238E+03	2.0886E-03	–	0†
60	CH_{3el}	C:1, H:3	-1.0830E+03	2.1109E-03	–	0†
61	$LiOCH_2CH_{3el}$	Li:1, C:, H:5, O:1	-4.4066E+03	3.0949E-03	–	0†
62	$LiCH_3CH_2OCO_{el}$	Li:1, C:3, H:5, O:2	-7.4901E+03	3.5882E-03	–	0†
63	$LiCH_3OCO_{el}$	Li:1, C:2, H:3, O:2	-6.4208E+03	3.3248E-03	–	0†
64	$LiDEC_{el}$	Li:1, C:5, H:10, O:3	-1.1691E+04	4.5265E-03	–	0†
65	LEC_{el}	Li:1, C:3, H:5, O:3	-9.5398E+03	3.6638E-03	–	0†
66	C_2H_{5el}	C:2, H:5	-2.1523E+03	2.5879E-03	–	0†
67	$PEC\_PEO\_dimer_{el}$	Li:2, C:5, H:8, O:5	-1.5961E+04	5.0178E-03	–	0†
68	$LiFEC\_lessH^+_{el}$	Li:1, C:3, F:1, H:2, O:3, E:-1	-1.2201E+04	3.7985E-03	–	0†
69	$LiFEC\_RO_{el}$	Li:1, C:3, H:3, O:3	-1.2221E+04	3.8802E-03	–	0†
70	$LiPC_{el}$	Li:1, C:4, H:6, O:3	-1.0590E+04	3.6992E-03	–	0†
71	$LiPC\_RO_{el}$	Li:1, C:4, H:6, O:3	-1.0591E+04	4.1638E-03	–	0†
72	$LiBC_{el}$	Li:1, C:5, H:8, O:3	-1.1659E+04	4.1902E-03	–	0†
73	$LiBC\_RO_{el}$	Li:1, C:5, H:8, O:3	-1.1660E+04	4.4794E-03	–	0†
74	$LiTetra_{112el}$	Li:1, C:5, H:11, O:4	-1.3755E+04	4.8286E-03	–	0†
75	$LiTetra_{122el}$	Li:1, C:6, H:13, O:4	-1.4824E+04	5.1759E-03	–	0†
76	$PEC\_dimer\_closed^-_{el}$	Li:1, C:5, H:8, O:5, E:1	-1.5757E+04	4.2438E-03	–	0†
77	$PEC\_dimer\_open\_Li_{el}$	Li:1, C:5, H:8, O:5, E:1	-1.5757E+04	4.3954E-03	–	0†
78	$FEC\_dimer^-_{el}$	C:5, F:1, H:6, O:4, E:1	-1.6188E+04	4.2557E-03	–	0†

* Values from Colclasure et al. [9]. † Species is considered minor and does not exceed 1E-4 kmol m^{-3} concentration at surface node with diffusion deactivated.
‡ Chosen to be favorable to deposit solid-phase species. ∥ Assumed.

13

have equilibrium potentials of 1.01 V (LiFEC$^+$), 0.81 V (LiEC$^+$), and 0.66 V (LiEMC$^+$). When simulating a voltage hold, these equilibrium potentials govern how favorably an available electron will reduce a particular nearby Li-coordinated species, as opposed to a different nearby Li-coordinated species.

Once a Li-coordinated species is reduced, several decomposition pathways are made available (see Fig. 2), which may include additional reduction of decomposed species. Competition between different decomposition routes is determined primarily by the reaction energy barriers. Figure 2 illustrates these homogeneous barriers for each reaction as $\Delta G^{\ddagger}$ in eV. For example, reduced LiEMC ([S18] in Fig. 2) has four available pathways to form either LEC, LMC, or decompose to form transesterification intermediates. The kinetic barriers for these routes are 0.66 eV (LEC), 0.70 eV (LMC), or 0.44 eV and 0.48 eV to initiate transesterification. Because the barriers to form LEC and LMC are much higher than to initiate transesterification, the model predicts relatively small amounts of LEC and LMC as compared to transesterification decomposition products.

Finally, the mechanism is sensitive to the assumed solubility of intermediate/final species. In the present model, five species are selected to favorably deposit as SEI species: LEDC, Li$_2$CO$_3$, LEC, LMC, and LiF. Once a species is deposited in the SEI phase, further decomposition of this species in the electrolyte phase is prevented. For example, BC is formed from the decomposition of LMC. If LMC is assumed to favorably deposit as a SEI species, less BC is predicted to form in the electrolyte phase. The homogeneous reactions – including intramolecular, concerted, and metal-hopping reactions – are documented in the CANTERA input file, Fig. 2, Table S3, and Table S4.

4. Model calibration and results

Before predicting electrolyte decomposition and resultant SEI formation, the model is calibrated with experimentally measured voltage-hold irreversible leakage currents. Specifically, the diffusion coefficient of the electron in the SEI D_{e^-} is tuned such that the irreversible leakage current predicted by the model is on the same order of magnitude as the leakage current measured in experiments (normalized by the active material surface area). To match experimental responses, the electron diffusion coefficient through the SEI is assumed to be voltage-dependent. Once calibrated at a specified voltage, the model-predicted SEI and electrolyte species evolution is analyzed.

4.1. Voltage-hold experiment and interpretation

To calibrate the SEI model, a Si electrode (80 wt.% Paraclete Energy Silicon, 10 wt.% Timcal carbon (C45), 10 wt.% lithium polyacrylate (LiPAA) binder, $\approx$1.1 mg/cm^2 total coating loading) was tested in a half-cell (14 mm Si electrode punch, 9/16" Li foil punch, 40 μL Gen2F electrolyte, 30°C). Triplicate cells were run under the voltage-hold protocol (described below) for 180 hr at 100 mV, 175 mV, 250 mV vs. Li. The nominal Si particle size for these cells was 150 nm. The Li/Si half cells have a nominal discharge capacity of 2 mAh in the voltage window 100 mV - 750 mV. Calculated volume fractions of active material Si, conductive additive C45 and binder LiPAA are 37.75%, 5.79%, and 9.16%, respectively with a porosity of 47.3%.

The voltage-hold protocol starts with 3 formation cycles at C/10 between 100 mV and 750 mV. Subsequently, the half-cell is discharged to the designated hold potential on the 4th cycle and held at that potential for 180 hr. Analysis for terminal current is conducted by normalizing to the 3rd lithiation half-cycle capacity of Si (mA/mAh). For each voltage hold experiment, three cell replicates are run. Variability in capacities is observed in coin cell data between the coin cell triplicates with 100 mV dataset showing the largest spread. The averaged data shows a higher voltage hold capacity to normalization capacity ratio at low voltage holds (high Si state-of-charge). This behavior is expected, as there is a higher propensity for SEI formation at higher states of lithiation. Initially, the current magnitudes are high and have contributions from both reversible lithiation and irreversible parasitic SEI currents [36]. Reversible current decreases continuously until the current signature is comprised mostly of parasitic current. Consequently, there is a need to deconvolve reversible lithiation from parasitic currents for accurate comparison with the present multiphase, multispecies SEI model. The general trend for the deconvoluted irreversible current indicates that the 100 mV voltage-hold has the highest irreversible current and 250 mV has the least irreversible current. Section S3 describes the experimental capacity data and deconvolution algorithm.

Figure 3b illustrates the irreversible leakage current from the experiments and the predicted responses after D_{e^-} calibration. Figure 3a illustrates the predicted SEI thickness increase during the 180 hr voltage hold. The SEI has a growth rate that approximates $t^{1/2}$ trends, which is expected for (electron) diffusion-limited growth. Table 4 documents the calibrated SEI electron diffusion coefficient at different voltage holds. As illustrated, the model-predicted irreversible current
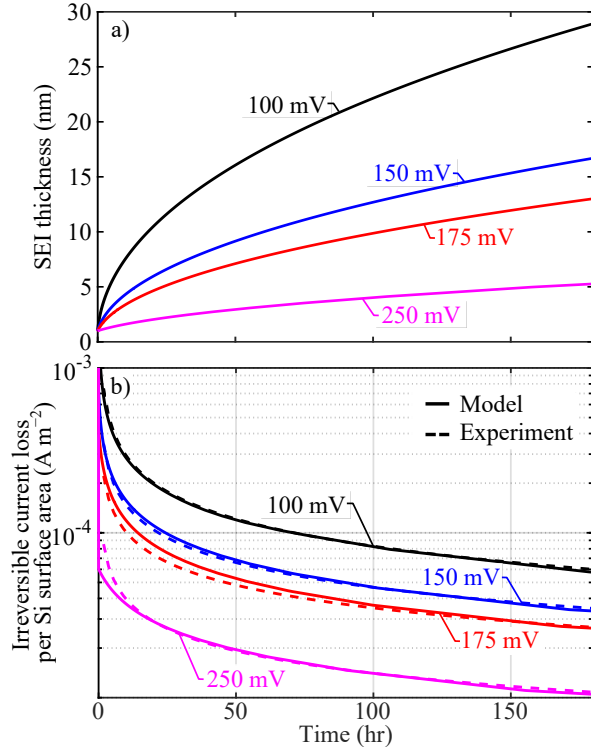
Figure 3: (a) Predicted SEI thickness dynamics for at each voltage during the 180 hr hold. (b) Measured irreverisble leakage current and model predicted responses at several voltage-holds of Si half-cells.

Table 4: Calibrated SEI electron diffusion coefficient at differet voltage holds.

Voltage-hold	$D_{e-}/(m^2\ s^{-1})$	SEI conductivity $\sigma_{SEI}\ /(\mu S\ m^{-1})$
100 mV	4.0E-18	1.17[†]
150 mV	1.2E-18	1.17[†]
175 mV	7.0E-19	1.17[†]
250 mV	1.0E-20	1.17[†]

[†] Conductivity is controlled by other charge species transport (i.e., V^-_{SEI}, Li^+_{SEI}).

accurately captures the change in magnitude and relative trends at each voltage hold.

4.2. Solid-phase species composition

Figure 4 illustrates the model-predicted evolution of the SEI species concentrations every 30 hr during a 100 mV, 180 hr voltage hold. All plots are shown as a function of normalized SEI thickness, where 0 indicates the electrode/SEI interface and unity indicates the SEI/electrolyte interface for all time (i.e., the responses are plotted w.r.t. the moving boundary variable ζ). Equation 10, Eqn. 11, and Fig. 3a can be used to translate the normalized distance (ζ and ξ) to the physical distance. As illustrated, with the current mechanism, a majority of the SEI consists of LEDC and LiF

(see Fig. 4e and Fig. 4c). Minor deposits of other structural species are predicted (i.e., Li_2CO_3, LMC, LEC). The modeled mechanism currently predicts that the SEI structural species concentrations after a 100 mV voltage hold are LiF > LEDC ≫ Li_2CO_3 > LEC > LMC. The minor deposits of some structural species (e.g., Li_2CO_3, LEC, and LMC) may indicate that there are too high of barriers or unfavorable species thermodynamics within the mechanism to form these expected SEI species, or that competing pathways are too favorable. For example, once reduced LiEC is formed, minimal kinetic barriers are predicted for [S45] to form (see Fig. 2 and Table 3) and to ultimately form LEDC by consuming CO_2. An alternative, competing pathway to form Li_2CO_3 from reduced LiEC has significant barriers ($\Delta G^{\ddagger} = 0.4$ eV) and has additional competing reactions that favor LEDC formation over Li_2CO_3 formation (see [S41] → [S43] decomposition routes in Fig. 2). Most SEI structural species (i.e., LEDC, LiF, LMC, and LEC) reach equilibrium concentrations after ≈30 hr. The only structural species that has significant concentration changes after ≈30 hr is Li_2CO_3. This indicates that as the SEI gets thicker and the irreversible leakage current decreases (see Fig. 3), the pathway to form Li_2CO_3 becomes less favorable for the limited available electrons as compared to pathways that form LEDC and LiF.

Importantly, the present manuscript documents a chemically complex SEI model using atomistically informed mechanisms. The model is expressed generally to accept any proposed mechanism. Feedback between experimental results and mechanism inputs will be explored in future work. Resulting adjustments to the model framework may include, for example, introducing homogeneous reactions in the SEI phase to further decompose LEDC to form additional Li_2CO_3, Li_2O, and gas-phase products.

Figure 4a illustrates the electron concentration in the SEI. At the SEI/electrolyte interface ($\zeta = 1$), the electron concentration is small. This indicates that the heterogeneous reactions are relatively fast at this interface and any available electrons are consumed. These dynamics suggest that SEI growth rate and irreversible currents are governed by electron diffusion. Importantly, operating in a diffusion-limited regime implies that model's sensitivity to heterogeneous reduction barriers is small.

Figure 4 shows that the model predicts an inorganic (LiF)-rich inner layer and a mixed organic (LEDC)/inorganic (LiF) outer layer. In this case, the inorganic-rich inner layer composition and thickness is strongly influenced by the assumed initial condition of
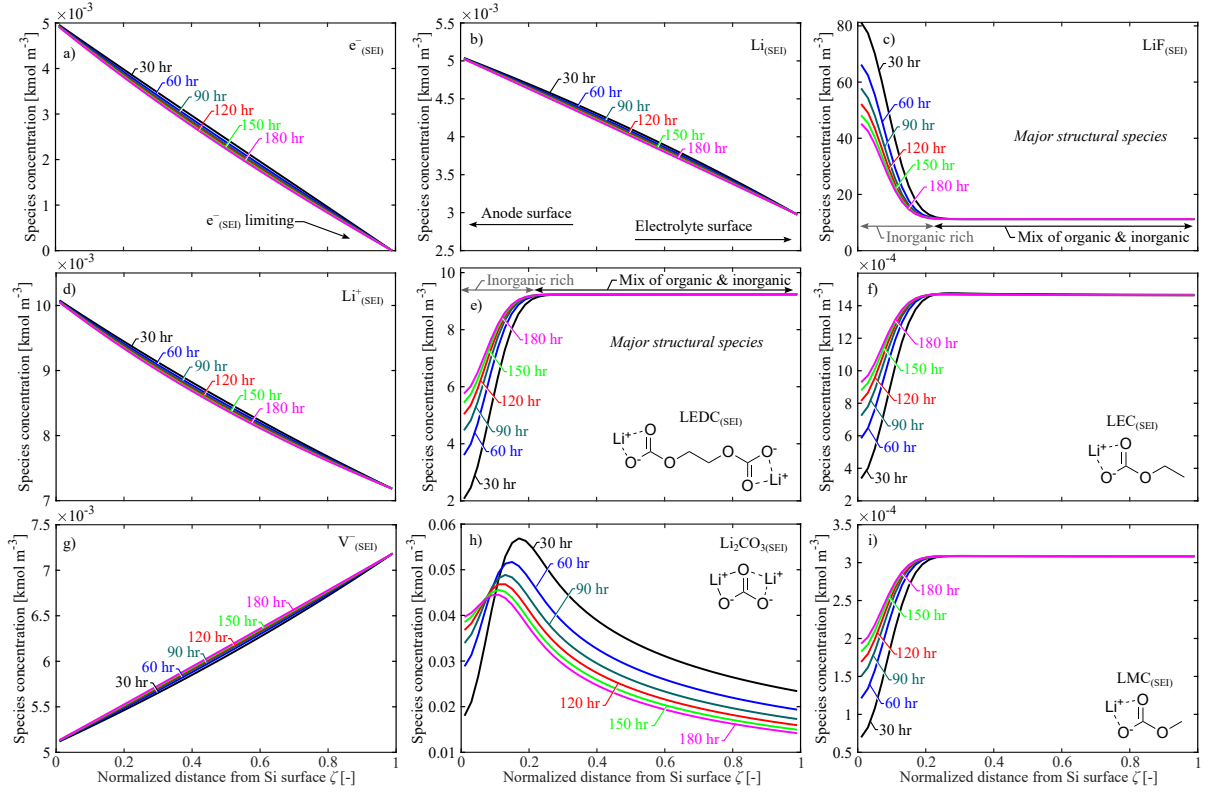
Figure 4: Predicted SEI species concentrations during a 100 mV, 180 hr voltage hold. Responses are shown at every 30 hr during the hold.

a 1 nm thick SEI of LiF. Instead of assigning an inner inorganic layer through initial conditions, the present model can evolve such an inner layer by ramping the voltage from a high value to a low value. A ramped voltage profile results in favorable LiFEC$^+$ reduction (E^{eq} = 1.012 V) as opposed to LiEC$^+$ or LiEMC$^+$ reduction (E^{eq} = 0.810 V and E^{eq} = 0.663 V, respectively, cf. Table S2). Favoring the LiFEC$^+$ reduction pathway will result in more LiF formation, which can deposit before reducing the voltage further to then favor LEDC formation. Achieving an inorganic LiF inner layer is fairly straightforward when a voltage between 1.012 V and 0.810 V is specified. However, achieving an organic outer layer is more complex. After forming the inner layer, if the model is held below 0.810 V, both competing reduction pathways for LiEC$^+$ and LiFEC$^+$ become active to form LEDC and LiF, respectively. In this case, the model predicts a mixture of organic and inorganic species in the outer layer (see Fig. 4c and Fig. 4e). To achieve an inorganic-rich outer layer at these low voltages, where LiFEC$^+$ reduction is also favorable, requires one or more of the following hypothetical conditions: 1) The FEC additive is sufficiently

consumed that it is no longer a significant species in the bulk electrolyte; 2) Once LEDC is deposited, the relative solubility of LEDC in solution is decreased and the solubility of LiF in solution is increased; 3) The presence of LEDC in the SEI increases the favorability of EC and EMC reduction over FEC reduction; and/or 4) The thermodynamics of solid-phase species is such that late-forming LiF diffuses to the inner inorganic layer (similar to phase segregation). Further complex boundary conditions and additional physics (see Section 5) are beyond the current scope of the manuscript, but will be considered in future work.

4.3. Electrolyte-phase species composition

Figure 5 and Figure S1 illustrate predicted species concentrations every 30 hr during a 180 hr voltage hold at 100 mV. All species are plotted with respect to the normalized distance from the SEI interface out to R_{el} = 2 μm (i.e., the responses are plotted w.r.t. ξ). The model simulates 39 mobile species that evolve in space and time (see Table 3)[2]. Only a select few species are

---

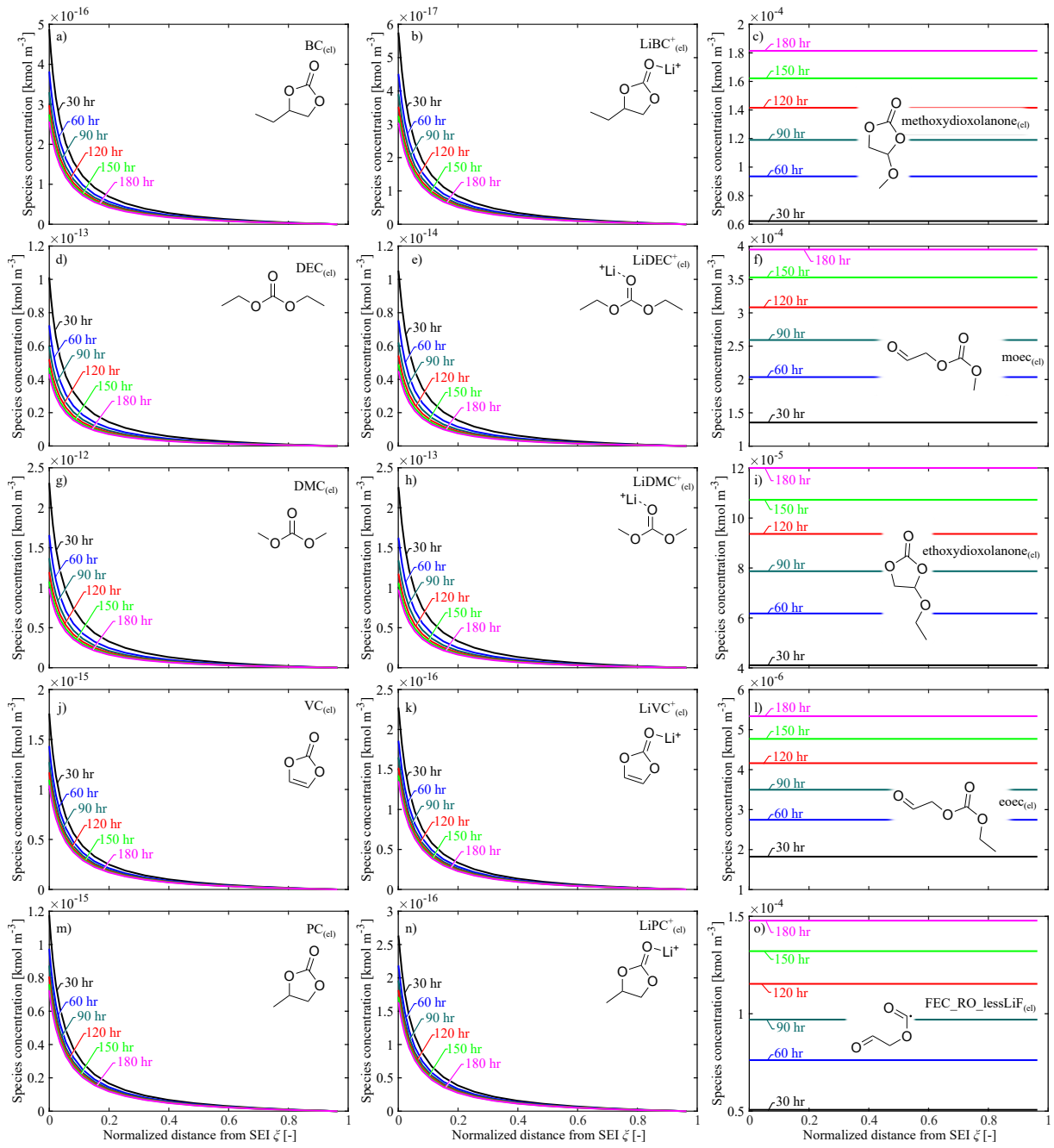[2]Additional intermediate species are simulated with respect to only time (see Table 3)

Figure 5: Predicted selected electrolyte species concentrations during a 100 mV voltage hold. Responses are shown for 30 hr, 60 hr 90 hr, 120 hr, 150 hr, and 180 hr into the hold.

plotted here. Figure 5 illustrates additional select electrolyte species concentrations. The species concentrations indicate that at the SEI/electrolyte interface (left side of Fig. 5) the initial electrolyte species are consumed and decomposition products (e.g., DMC, DEC) are produced. At early times, more current is available at the SEI interface, which results in more reduction reactions, which results in more consumption/production of electrolyte species. As the SEI thickness increases (Fig. 3a), the irreversible current decreases, which results in less overall reactivity.

Figure 5 illustrates two predominant electrolyte dy-

namics. The left and middle plots show species forming at the SEI interface and diffusing away from the SEI interface. At early times, higher species concentrations are predicted; at later times when the SEI has grown and there is less irreversible current, fewer species are formed at the interface. Since these species are further consumed (see Fig. 2), they do not accumulate in the electrolyte phase. The species illustrated on the right have different dynamics than the species plotted on the left and in the center. Specifically, the species on the right are considered "final" in the mechanism, i.e., there are no reactions that consume these species favorably (note that all reactions are expressed as reversible). Because these species are not readily consumed, they accumulate in the electrolyte phase during the 180 hr hold. Figure S1 illustrates additional electrolyte species formed during a 100 mV/180 hr voltage hold, including gas-phase species dissolved in the electrolyte (Figure S1a-i). Under the present mechanism, all gas species are found to increase during the voltage hold.

5. Discussion

The primary goal of the present manuscript is to document a continuum-level model that can communicate atomistic knowledge (e.g., reaction pathways, rates, species transport properties) to time- and length-scales that are experimentally relevant. Additionally, the present model is meant to act as a bridge to validate (electro)chemical mechanisms proposed from experimentally observed signals. More specifically, it is common for the atomistic modeling community to propose reaction networks, decomposition rates, species transport properties, etc. that seek to explain initial Li-ion SEI formation. However, translating these predictions to long timescales has been challenging, preventing significant experimental validation. Additionally, it is common for the experimental community to detect atom/bond/molecule signals and propose (typically global) reactions that would logically produce these measured signals [107, 108]. However, the mechanisms proposed from experimental observation are not typically predictive, i.e., they struggle with answering: "What would occur if additive X was included in the system?".

5.1. Strengths of the present approach

A major strength of the present continuum-level model is its ability to operate bidirectionally, such that atomistic insights can be upscaled to experimentally measurable signals and experimental observations can be used to refine atomistic insights. In particular, the model framework enables the use of first-principles atomistic insights to deconvolute competing reaction pathways that produce the same resultant species. Such deconvolution has traditionally challenged the experimental community. For example, vinylene carbonate (VC) is a well-documented component present in aged electrolyte whose origin is typically attributed to FEC and/or EC reduction [107, 109, 110]. Multiple distinct mechanistic pathways have been proposed that could feasibly result in VC evolution, and which are supported by complementary experimental analysis. Notable proposed mechanisms include the reaction of FEC with alkoxide products and the concurrent loss of HF to form VC and LiF [111, 112], or alternatively the radical disproportionation of EC to form VC [113, 114]. The "correct" mechanistic attribution for VC formation remains contested in the experimental literature [110], as well as consumption of VC to form additional species. CO_2 presents a similar challenge, with experimentally supported pathways to produce (and consume) CO_2 associated with all standard electrolyte solvents, as well as multiple downstream intermediates and – in the case of Li metal anodes – even the electrode surface itself [115].

Clearly, for such complex systems, deconvolution of all potential pathways based solely on (electro)chemical intuition is impractical. It is also unfeasible to attempt deconvolution through precise experimental detection of all complementary evolved species, when the number of relevant species is on the order of dozens to hundreds across three phases. The model, thus, offers a complementary approach to experimental measurements, whereby the favorability of competing and complex mechanistic pathways can be evaluated to both explain and help predict experimental observations.

Further, the model offers a flexible framework to capture SEI-forming reactions in all three phases. The inclusion of dissolved gas species in particular, which is likely under-explored in battery research, is unique to this model, and represents a substantial advancement in terms of realistically representing SEI behavior. The continuum model itself is somewhat mechanism-agnostic; i.e., the model may be tuned and validated on multiple different electrode and electrolyte systems and may be adjusted to incorporate varying mechanisms (as long as complete pathways and appropriate physical properties are provided).

It should be noted that the atomistic reaction network used in the present model demonstration has been developed in conjunction with experimental feedback, and as such successfully captures nuanced SEI reaction behav-

ior that has been omitted in previous simulations. For example, the transesterification reactions and associated products presented in Fig. 2 and described in Section 3.2 have been repeatedly reported and validated by experimentalists [116–119]. Interestingly, predicting reasonable irreversible current trajectories (see Fig. 3) when transesterification reactions are present required pathways to ultimately deposit solid-phase species (see reactions labelled "FEC & Transesterifcation Intermediates" in Fig. 2). EMC reduction and decomposition to transesterification products produces soluble species (i.e., DMC and DEC). As a result, a significant portion of the irreversible current was taken up in bulk electrolyte changes and very little contributed to SEI formation. If the reactions with transesterification intermediates and FEC are not included in the mechanism, then the SEI growth rate is significantly reduced (less LiF is formed) and the irreversible currents are more linear with respect to time as opposed to exhibiting a more $t^{1/2}$ trajectory. Such pathways to "scavenge" alkoxide intermediates and form LiF have in fact been reported and validated in the experimental literature [118], and are captured in the present atomistic mechanism. The complexity and breadth of reaction pathways incorporated into the model is unprecedented; this facilitates improved resolution in reflecting observed (electro)chemical reactivity.

5.2. Additional SEI physics in next-generation anodes

The continuum-level model has been developed with a specific emphasis on evaluating the passivation behavior of next-generation anodes. To this end, the model has been tuned and validated on Si-based Li-ion cell chemistry. A somewhat confounding observation when considering SEI formation and passivation is the obvious difference between SEI passivation on graphite and the lack of passivation on Si and Li surfaces. Further, while both Si and Li electrodes have significantly more volume-change on cycling than graphite, Si and Li surfaces themselves seem to have different passivation characteristics. For example, Li metal has rapid cycling fade [8], while nano-Si can cycle for hundreds to thousands of cycles, but has reduced calendar-life [17]. The following section discusses remaining challenges in understanding and simulating SEI formation in next-generation Li-ion battery materials. Some of these challenges can be addressed by the current chemically complex continuum-level model framework, while others may require incorporating additional physics. Such modifications are possible within the inherently flexible model framework, although the complexity of physics required to capture certain behaviors is high in several cases. The additional phenomena considered below are listed in rough order of increasing intensity of the adjustment(s) that would be required for the present model framework to capture.

1. *Additional reactive pathways.* As noted in Table 1, the present model and associated atomistic reaction network together represent the most chemically complex continuum-level model reported to date. However, even with the addition of orders of magnitude more chemical complexity, it is unrealistic to suggest that all possible chemical pathways will be captured. In the case of the next-generation anodes (e.g., Si and Li), important additional reactive pathways include salt decomposition; reactions of trace water; and homogeneous SEI-phase reactions (i.e., continued reactivity of species following deposition).

The nature of the salt has been experimentally demonstrated to drastically influence the resulting SEI composition, particularly since salt decomposition is believed to contribute to the formation of the "pre-SEI" layer [11] (herein assigned via initial condition to be a 1 nm layer of LiF). Further, even in the most carefully prepared systems, the presence of trace water has been detected in both the electrolyte and as hydration water within the electrodes. Water and other protic contaminants are reported to hydrolyze electrolyte solvents at high reduction potentials [118, 120], and in the case of Si, HF formed through reactions between water and $LiPF_6$ salt can directly etch the Si surface [11, 120]. Finally, the reported changes to SEI composition and morphology over repeated cycling of next-generation cells suggest that homogeneous reactions may be occurring within the SEI solid phase. Of these additional reactive pathways, incorporating salt decomposition is perhaps the most readily accessible, and this effort is already underway. Including water introduces drastically expanded mechanistic complexity and is likely to introduce numerical stability challenges, since water readily reacts with nearly all electrolyte species initially present in the system, as well as many of the reactive intermediates and products. Incorporating homogeneous SEI reactions is feasible, but would require first-principles calculations and/or experimental measurements of the thermodynamic properties and kinetic barriers to form SEI products, many of which have not yet even been conclusively identified.

2. *Capturing additional SEI dynamics.* In the present continuum-level model framework, although all reactions are fundamentally reversible, the species ther-

modynamics of primary deposition products has been chosen such that deposition is thermodynamically favorable, i.e., the SEI only grows. However, there is experimental evidence for dynamic SEI deposition/dissolution under conditions of both electrode cycling and storage [11, 94]. In next-generation Si and Li materials, the electrode surface is also believed to (electro-)chemically react with the SEI, such that the SEI grows into the underlying electrode active material. Specifically for Si, cryogenic scanning transmission electron microscopy (cryo-STEM) and energy dispersive X-ray spectroscopy (EDS) elemental mapping have recently shown that the expected core-shell structure for the Si-SEI is seen after the first cycle, but after sufficient cycling, the Si-SEI becomes increasingly blended [121]. This behavior is in contrast to graphite, where it is believed that the SEI surface layer does not react with the underlying C_6 structure and a core-shell structure is maintained [9, 61, 69, 122]. The SEI's inward growth on Si may cause additional capacity fade. In the continuum-level modeling framework, treating the first of these additional SEI dynamics (i.e., including dissolution as well as deposition) is relatively straightforward. However, this requires formulation of additional inputs including solubility values and kinetic barriers of various complex reduction products. Incorporating SEI blending with the underlying electrode would involve introducing an additional reactive boundary, which would be handled similarly to the SEI/electrolyte boundary. Instead of assuming only electrons and Li cross the electrode/SEI boundary, additional heterogeneous reactions could occur that eat away at the electrode structure and "blend" the SEI with the electrode. Adding this additional reactive boundary requires a robust understanding of the relevant heterogeneous solid-solid reactions, which is difficult to predict from first principles (see Section 1.1), and a possible reformulation to handle two moving boundaries (at the Si/SEI and SEI/electrolyte interfaces) as opposed to one (at the SEI/electrolyte interface).

3. *Chemo-mechanics.* In contrast to graphite, which undergoes relatively minor volume-change dynamics, the substantial volume change occurring in both Li and Si can influence SEI passivation via SEI cracking or thinning. However, the connection between electrode strain and SEI growth dynamics is not straightforward. In the case of Li metal, there is an "infinitely large volume expansion" [8], and in the case of Si, lithiation results in an expansion

of $\approx 280\%$ [18]. If these large volume changes influence SEI growth, the volume-change dependence would most likely influence cycling performance. This conclusion is supported by the reduced cycle life observed in Li-metal electrodes. For Si, efforts have been made to mitigate these volume-change effects by reducing the active particle size to the nanoscale [123]. Such nano-Si materials demonstrate improved cycle life but still suffer from reduced calendar life, likely due to the highly increased surface-to-volume ratios realized by the stress-reducing nanostructures. Thus, volume-change behavior alone cannot fully explain why Si exhibits reduced calendar life, since the Si expansion/contraction is relatively small during calendar-aging as compared to the expansion/contraction during cycle-aging. Including simulated finite-strain chemo-mechanics on the particle- and electrode-levels [20, 124, 125] may be necessary for the continuum-level model framework to fully capture the factors influencing SEI stability. Such addition of chemo-mechanics is not the focus of the present model - which emphasizes upscaling significantly complex reaction networks from atomistic theory - but future iterations will include finite-strain chemo-mechanics.

4. *Surface chemistry sensitivities.* One hypothesis for the differences in passivation behavior between graphite and Si or Li is that the chemical interface (Si, SiO_x, or Li) exposed to the electrolyte influences the decomposition pathway. Such an argument would be supported by first-principles MD simulations that predict surface termination strongly influences initial electrolyte decomposition [31, 126]. Surface sensitivity is supported in experimental studies where surface termination is found to influence the composition of the gas-phase species resulting from electrolyte decomposition [127]. Furthermore, the introduction of carbon to the silicon surface is found to affect interfacial reactivity. For example, two-dimensional silicene structures show improved performance when covered by a thin layer of covalently bound graphene [128].

However, other measurements indicate that long-term side reactions seem to be less sensitive to electrode surface termination, and instead, are more sensitive to the initial SEI composition (e.g., whether LiF formed) [32]. Continuing the arguments against surface-termination sensitivity, Yu et al. [129] used DFT and MD to simulate EC decomposition on graphite and Li-metal and argued that EC decomposition is analogous on both surfaces, but faster for the Li surface. Logically, the surface chemistry may in-

20

fluence the initial electrolyte decomposition, but after an initial surface layer is formed, the underlying electrode chemistry becomes (chemically) inconsequential unless the underlying electrode/surface layer break apart and fresh electrode surface is exposed; for example, if Si cracks during cycling (not likely for calendar aging though). Instead, any long-term surface mediated reactions must involve the initially formed SEI layer. Since graphite doesn't initially form a chemically significant different SEI than either Si or Li, it is unlikely that the surface termination of the underlying electrode has a strong effect on SEI passivation.

The reported model framework is somewhat surface-agnostic, whereby the surface is treated as an electron source and reaction favorability is driven by the availability of electrons, which is a function of potential and electron/Li diffusion through the growing SEI. At present, the model cannot readily explain or predict the differences in passivation between graphite and Si or Li anodes. Ongoing efforts are underway to determine appropriate treatment of surface chemistry, and evaluate how varying surface terminations may influence the magnitude of reaction barriers.

5. *Non-molecular species reactivity.* Finally, recent experimental studies using isotopic labeling to evaluate gaseous decomposition products have challenged the fundamental assumption of molecular species reactivity [119, 130]. Specifically, there is experimental evidence that atomic "cross-reactivity" occurs during both electrolyte-phase [119] and gas-phase [130] reactions, such that a given product species may contain, for example, carbon atoms originating from EC and hydrogen atoms originating from EMC. This novel proposed behavior has not been considered by the atomistic mechanism. To capture such physics would require substantially more complex reaction networks and appropriate isotope labeling in the Cantera input file, and is beyond the scope of the present effort – but may be an interesting avenue for future expansion.

5.3. Future model/mechanism validation

The present manuscript showcases capabilities to upscale atomistically informed mechanisms to continuum-level time- and length-scales relevant for studying the SEI. Once upscaled, the model can be validated by using experiments that detect solid-phase composition [23, 94, 120, 131–136], liquid-phase composition, and gas-phase composition [115, 134, 136–138]. These detection techniques can serve as a feedback mechanism

to refine the atomistically informed thermodynamics, pathways, transport, and kinetics.

A key challenge for the model is the need for several (potentially unknown) properties. For example, to validate the solid-phase composition, the model requires thermodynamics and kinetics for deposition/dissolution reactions. Additionally, if there are homogeneous reactions occurring within the SEI [120, 136], associated pathways, thermodynamics, and barriers are required (alongside species molar volumes). Similarly, to validate the gas-phase production, the species-specific solubility is required to communicate the species concentration in the electrolyte-phase to species concentrations in the gas-phase [139–141]. Future work will include model/mechanism validation with gas-phase detection techniques after voltage-holds alongside required species solubility measurements.

6. Summary and Conclusion

A chemically complex, continuum-level, single-particle Li-ion model is developed to understand electrolyte decomposition and solid-electrolyte interface formation on a Si nano-particle. The model considers facile decomposition for EC, EMC, and FEC to form common SEI species (e.g., LEDC, Li_2CO_3, LiF) and gaseous byproducts (e.g., CO, CO_2, CH_4, C_2H_2, C_2H_4, C_2H_6, C_3H_6, C_3H_8, and C_4H_8). The model is expressed generally to accept any atomistically informed reaction mechanism. In total, the model considers 9 SEI species, 22 heterogeneous reactions at the SEI/electrolyte interface, 149 electrolyte homogeneous reactions, and 78 electrolyte species.

The model is used to predict electrolyte and SEI composition during a 180 hr voltage hold. After calibration, the model correctly captures the irreversible leakage currents due to parasitic reactions at a variety of voltage-holds (e.g., 100 mV, 150 mV, 175 mV, and 250 mV). With the current mechanism, the model predicts significant LEDC and LiF formation as compared to other SEI species (i.e., Li_2CO_3, LEC, LMC). Additionally, the model predicts that the SEI grows at a square-root-of-time rate due to electron diffusion-limited transport through the SEI. The model is expected to be a key tool to communicate between atomistic predictions and experiment observations.

7. Acknowledgements

Nomenclature

Variable	Description	SI Units
A	Dummy dependent variable	–
C	Total lattice-site concentration	kmol m^{-3}
D_k	Species k diffusion coeff.	$\text{m}^2\,\text{s}^{-1}$
E^{eq}	Equilibrium potential	V
F	Faraday's constant	s A kmol^{-1}
ΔG	Reaction free energy	J kmol^{-1}
$\Delta G^{\ddagger}$	Reaction kinetic barrier	J kmol^{-1}
h	Planck's constant	$\text{kg m}^2\,\text{s}^{-1}$
$\mathbf{i}$	Current density	A m^{-2}
$\mathbf{J}_k$	Species k flux	$\text{kmol m}^{-2}\,\text{s}^{-1}$
k_{B}	Boltzmann constant	$\text{kg m}^2\,\text{s}^{-1}\,\text{K}^{-1}$
k_{f}	Forward reaction rate	kmol, m, s
$\mathbf{n}$	Surface normal	–
R	Universal gas constant	$\text{J kmol}^{-1}\,\text{K}^{-1}$
R_{el}	Electrolyte domain radius	m
R_{min}	Min electrode distance for hetero. reactions	m
r	Independent radial variable	m
r_{p}	Anode particle radius	m
$\dot{s}_k$	Net surface production rate of species k	$\text{kmol m}^{-2}\,\text{s}^{-1}$
t	Time	s
T	Temperature	K
$\mathbf{v}$	Bulk velocity	m s^{-1}
$[X_k]$	Species concentration	kmol m^{-3}
W_k	Molecular weight of species k	kmol kg^{-1}
z_k	Species k charge	–

β	Sensitivity term in reduction reactions	m^{-1}
Γ	Reaction scaling variable	–
δ	SEI thickness	m
ζ	Independent radial variable in the SEI	–
κ_{ET}	Electron transfer forward rate	s^{-1}
$\kappa_{\text{surf,ET}}$	Total surface reaction rate	m s^{-1}
κ_0	Tunneling coefficient pre-factor	–
λ	Reorganization energy	J kmol^{-1}
λ_{inner}	Inner reorganization energy	J kmol^{-1}
λ_{outer}	Outer reorganization energy	J kmol^{-1}
μ_k°	Species k standard-state chemical potential	J kmol^{-1}
ξ	Independent radial variable in the electrolyte	–
ρ_k	Species k density	kg m^{-3}
σ	Electronic conductivity	S m^{-1}
τ	Transformed independent time variable	s
Φ	Potential	V
$\dot{\omega}_k$	Volumetric production rate of species k	$\text{kmol m}^{-3}\,\text{s}^{-1}$

References

[1] M. Li, J. Lu, Z. Chen, and K. Amine. 30 years of lithium-ion batteries. *Adv. Mater.*, 30:1800561, 2018.

[2] J.B. Goodenough and Y. Kim. Challeges for rechargeable Li batteries. *Chem. Mater.*, 22:587–603, 2010.

[3] S.J. An, J. Li, C. Daniel, D. Mohanty, S. Nagpure, and D.L. Wood III. The state of understanding of the lithium-ion-battery graphite solid electrolyte interface (SEI) and its relationships to formation cycling. *Carbon*, 105:52–76, 2016.

[4] K. Xu. Nonaqueous liquid electrolytes for lithium-based rechargeable batteries. *Chem. Rev.*, 104:4303–4418, 2004.

[5] K. Xu. Electrolytes and interphases in Li-ion batteries and beyond. *Chem. Rev.*, 114:11503–11618, 2014.

[6] J. Nanda, G. Yang, T. Hou, D.N. Voylov, X. Lin, R.E. Ruther, M. Naguib, K. Persson, G.M. Veith, and A.P. Sokolov. Unraveling the nanoscale heterogeneity of solid electrolyte interphase using tip-enhanced raman spectroscopy. *Joule*, 3:2001–2019, 2019.

[7] D. Zhao and S. Li. Regulating the performance of lithium-ion battery focus on the electrode-electrolyte interface. *Front. Chem.*, 8:821, 2020.

[8] B. Horstmann, J. Shi, R. Amine, M. Werres, X. He, H. Jia, F. Hausen, I. Cekic-Laskovic, S. Wiemers-Meyer, J. Lopez, D. Galvez-Aranda, F. Baakes, D. Bresser, C.-C. Su, Y. Xu, W. Xu, P. Jakes, R.-A. Eichel, E. Figgemeier, U. Krewer, J.M. Seminario, P.B. Balbuena, C. Wang, S. Passerini, Y. Shao-Horn, M. Winter, K. Amine, R. Kostecki, and A. Latz. Strategies towards enabling lithium metal in batteries: interphases and electrodes. *Energy Environ. Sci.*, 14:5289–5314, 2021.

[9] A.M. Colclasure, K.A. Smith, and R.J. Kee. Modeling detailed chemistry and transport for solid-electrolyte-interface (SEI) films in Li-ion batteries. *Electrochim. Acta*, 58:33–43, 2011.

[10] X. He, D. Bresser, S. Passerini, F. Baakes, U. Krewer, J. Lopez, C.T. Mallia, Yang S.-H., I. Cekic-Laskovic, S. Wiemers-Meyer, F.A. Soto, V. Ponce, J.M. Seminario, P.B. Balbuena, H. Jia, W. Xu, Y. Xu, C. Wang, B. Horstmann, R. Amine, C.-C. Su, J. Shi, K. Amine, M. Winter, A. Latz, and R. Kostecki. The passivation of lithium electrodes in liquid electrolytes for secondary batteries. *Nat. Rev. Mater.*, 6:1036–1052, 2021.

[11] G.M. Veith, M. Doucet, R.L. Sacci, B. Vacaliuc, J.K. Baldwin, and J.F. Browning. Determination of the solid-electrolyte interface structure grown on a silicon electrode using a fluoroethylene carbonate additive. *Sci. Rep.*, 7:6326, 2017.

[12] R.T. Pekarek, A. Affolter, L.L. Baranowski, J. Coyle, T. Hou, E. Sivonxay, B.A. Smith, R.D. McAuliffe, K.A. Persson, B. Key, C. Apblett, G.M. Veith, and N.R. Neale. Intrinsic

chemical reactivity of solid-electrolyte interphase components in silicon–lithium alloy anode batteries probed by FTIR spectroscopy. *J. Mater. Chem. A*, 8:7897–7906, 2020.

[13] Y. Jin, B. Zhu, Z. Lu, N. Liu, and J. Zhu. Challenges and recent progress in the development of Si anodes for lithium-ion battery. *Adv. Energy Mater.*, 7:1700715, 2017.

[14] J.E. Harlow, X. Ma, J. Li, E. Logan, Y. Liu, N. Zhang, L. Ma, S.L. Glazier, M.M.E. Cormier, M. Genovese, S. Buteau, A. Cameron, J.E. Stark, and J.R. Dahn. A wide range of testing results on an excellent lithium-ion cell chemistry to be used as benchmarks for new battery technologies. *J. Electrochem. Soc.*, 166(13):A3031–A3044, 2019.

[15] I. Hasa, A.M. Haregewoina, L. Zhang, W.-Y. Tsai, J. Guo, G.M. Veith, P.N. Ross, and R. Kostecki. Electrochemical reactivity and passivation of silicon thin-film electrodes in organic carbonate electrolytes. *ACS Appl. Mater. Interfaces*, 12:36, 2020.

[16] Y. Zhang, X. Li, E. Sivonxay, J. Wen, K.A. Persson, J.T. Vaughey, B. Key, and F. Dogan. Silicon anodes with improved calendar life enabled by multivalent additives. *Adv. Energy Mater.*, 11:2101820, 2021.

[17] J.D. McBrayer, M.-T.F. Rodrigues, M.C. Schulze, D.P. Abraham, C.A. Apblett, I. Bloom, G.M. Carroll, A.M. Colclasure, C. Fang, K.L. Harrison, G. Liu, S.D. Minteer, N.R. Neale, G.M. Veith, C.S. Johnson, J.T. Vaughey, A.K. Burrell, and B. Cunningham. Calendar aging of silicon containing batteries. *Nat. Energy*, 6:866–872, 2021.

[18] M.N. Obrovac and V.L. Chevrier. Alloy negative electrodes for Li-ion batteries. *Chem. Rev.*, 114(23):11444–11502, 2014.

[19] X.H. Liu, Z. Huang, S.X. Mao, T. Zhu, and J.Y. Huang. Size-dependent fracture of silicon nanoparticles during lithiation. *ACS Nano*, 6(2):1522–1531, 2012.

[20] L. von Kolzenberg, A. Latz, and B. Horstmann. Chemomechanical model of SEI growth on silicon electrode particles. *Batter. Supercaps*, 5:e202100216, 2022.

[21] T. Shen, Z. Yao, Z. Xia, X. Wang, C. Gu, and J. Tu. Rationally designed silicon nanostructures as anode material for lithium-ion batteries. *Adv. Energy Mater.*, 20:1700591, 2018.

[22] K. Kalaga, M.-T.F. Rodrigues, S.E. Trask, I.A. Shkrob, and D.P. Abraham. Calendar-life versus cycle-life aging of lithium-ion cells with silicon-graphite composite electrodes. *Electrochim. Acta*, 280:221–228, 2018.

[23] T.F. Malkowski, Z. Yang, R.L. Sacci, S.E. Trask, M.-T.F. Rodrigues, I.D. Bloom, and G.M. Veith. Evaluating the roles of electrolyte components on the passivation of silicon anodes. *J. Power Sources*, 523:231021, 2022.

[24] S. Jurng, Z.L. Brown, J. Kim, and B.L. Lucht. Effect of electrolyte on the nanostructure of the solid electrolyte interface (SEI) and performance of lithium metal anodes. *Energy Environ. Sci.*, 11:2600, 2018.

[25] Y. Li, W. Huang, Y. Li, A. Pei, D.T. Boyle, and Y. Cui. Correlating structure and function of battery interphases at atomic resolution using cryoelectron microscopy. *Joule*, 2:2167–2177, 2018.

[26] M. Haruta, T. Okubo, Y. Masuo, S. Yoshida, A. Tomita, T. Takenaka, T. Doi, and M. Inaba. Temperature effects on SEI formation and cyclability of Si nanoflake powder anode in the presence of SEI-forming additives. *Electrochem. Acta*, 224:186–193, 2017.

[27] L.D. Ellis, J.P. Allen, I.G. Hill, and J.R. Dahn. High-precision coulometry studies of the impact of temperature and time on SEI formation in Li-ion cells. *J. Electrochem. Soc.*, 165(7):A1529–A1536, 2018.

[28] S. Das, P.M. Attia, W.C. Chueh, and M.Z. Bazant. Electrochemical kinetics of SEI growth on carbon black: Part II. Mod-

eling. *J. Electrochem. Soc.*, 166(4):E107–E118, 2019.

[29] A.L. Michan, M. Leskes, and C.P. Grey. Voltage dependent solid electrolyte interface formation in silicon electrodes: Monitoring the formation of organic decomposition products. *Chem. Mater.*, 28:385–398, 2016.

[30] C.K. Chan, R. Ruffo, S.S. Hong, and Y. Cui. Surface chemistry and morphology of the solid electrolyte interphase on silicon nanowire lithium-ion battery anodes. *J. Power Sources*, 189:1132–1140, 2009.

[31] K. Leung and J.L. Bedzien. Ab initio molecular dynamics simulations of the initial stages of solid–electrolyte interphase formation on lithium ion battery graphitic anodes. *Phys. Chem. Chem. Phys.*, 12:65383–6586, 2010.

[32] M.C. Schulze, G.M. Carroll, T.R. Martin, K. Sanchez-Rivera, F. Urias, and N.R. Neale. Hydrophobic versus hydrophilic interfacial coatings on silicon nanoparticles teach us how to design the solid electrolyte interphase in silicon-based Li-ion battery anodes. *ACS Appl. Energy Mater.*, 4(2):1628–1636, 2021.

[33] H. Wu, H. Jia, C. Wang, J.-G. Zhang, and W. Xu. Recent progress in understanding solid electrolyte interphase on lithium metal anodes. *Adv. Energy Mater.*, 11:2003092, 2021.

[34] A. Tornheim, S.E. Trask, and Z. Zhang. Evaluation of electrolyte oxidation stability on charged $LiNi_{0.5}Co_{0.2}Mn_{0.3}O_2$ cathode surface through potentiostatic holds. *J. Electrochem. Soc.*, 163:A1717, 2016.

[35] H. Gao, L. Xiao, I. Plümel, G.-L. Xu, Y. Ren, Z. Zuo, Y. Liu, C. Schulz, H. Wiggers, K. Amine, and Z. Chen. Parasitic reactions in nanosized silicon anodes for lithium-ion batteries. *Nano Lett.*, 17:1512–1519, 2017.

[36] M.C. Schulze, M.-T.F. Rodrigues, J.D. McBrayer, D.P. Abraham, C.A. Apblett, I. Bloom, Z. Chen, A.M. Colclasure, A.R. Dunlop, and C. Fang. Critical evaluation of potentiostatic holds as accelerated predictors of capacity fade during calendar aging. *J. Electrochem. Soc.*, 169:050531, 2022.

[37] T. Roth, L. Streck, A. Graule, P. Niehoff, and A. Jossen. Relaxation effects in self-discharge measurements of lithium-ion batteries. *J. Electrochem. Soc.*, 170:020502, 2023.

[38] A. Wang, S. Kadam, H. Li, S. Shi, and Y. Qi. Review on modeling of the anode solid electrolyte interface (SEI) for lithium-ion batteries. *Npj Comp. Mater.*, 4:15, 2018.

[39] C.W. Lee, N.H. Cho, S.W. Im, M.S. Jee, Y.J. Hwang, B.K. Min, and K.T. Nam. New challenges of electrokinetic studies in investigating the reaction mechanism of electrochemical CO_2 reduction. *J. Mater. Chem. A*, 6(29):14043–14057, 2018.

[40] X. Qu, A. Jain, N.N. Rajput, L. Cheng, Y. Zhang, S.P. Ong, M. Brafman, E. Maginn, L.A. Curtiss, and K.A. Persson. The electrolyte genome project: A big data approach in battery materials discovery. *Comput. Mater. Sci.*, 103:56–67, 2015.

[41] Y. Wang, S. Nakamura, M. Ue, and P.B. Balbuena. Theoretical studies to understand surface chemistry on carbon anodes for lithium-ion batteries: reduction mechanisms of ethylene carbonate. *J. Am. Chem. Soc.*, 123(47):11708–11718, 2001.

[42] K. Leung. Two-electron reduction of ethylene carbonate: A quantum chemistry re-examination of mechanisms. *Chem. Phys. Lett.*, 568:1–8, 2013.

[43] L.D. Gibson and J. Pfaendtner. Solvent oligomerization pathways facilitated by electrolyte additives during solid-electrolyte interphase formation. *Phys. Chem. Chem. Phys.*, 22(37):21494–21503, 2020.

[44] D. Kuai and P.B. Balbuena. Solvent degradation and polymerization in the li-metal battery: Organic-phase formation in solid-electrolyte interphases. *ACS Appl. Mater. Interfaces*, 14(2):2817–2824, 2022.

[45] E.W.C. Spotte-Smith, T.B. Petroceli, H.D. Patel, S.M. Blau, and K.A. Persson. Elementary decomposition mechanisms of

lithium hexafluorophosphate in battery electrolytes and interphases. *ACS Energy Lett.*, 8:347–355, 2023.

[46] E.W.C. Spotte-Smith, S.M. Blau, D. Barter, N.J. Leon, N.T. Hahn, N.S. Redkar, K.R. Zavadil, C. Liao, and K.A. Persson. Chemical reaction networks explain gas evolution mechanisms in Mg-ion batteries. *J. Am. Chem. Soc.*, 2023.

[47] D. Barter, E.W.C. Spotte-Smith, N.S. Redkar, A. Khanwale, S. Dwaraknath, K.A. Persson, and S.M. Blau. Predictive stochastic analysis of massive filter-based electrochemical reaction networks. *Digital Discovery*, 02:123–137, 2023.

[48] S.M. Blau, H.D. Patel, E.W.C. Spotte-Smith, X. Xie, S. Dwaraknath, and K.A. Persson. A chemically consistent graph architecture for massive reaction networks applied to solid-electrolyte interphase formation. *Chem. Sci.*, 12:4931–4939, 2021.

[49] X. Xie, E.W.C. Spotte-Smith, M. Wen, H.D. Patel, S.M. Blau, and K.A. Persson. Data-driven prediction of formation mechanisms of lithium ethylene monocarbonate with an automated reaction network. *J. Am. Chem. Soc.*, 143:13245–13258, 2021.

[50] E.W.C. Spotte-Smith, R.L. Kam, D. Barter, X. Xie, T. Hou, S. Dwaraknath, S.M. Blau, and K.A. Persson. Towards a mechanistic model of solid-electrolyte interphase formation and evolution in lithium-ion batteries. *ACS Energy Lett.*, 4:1446–1453, 2022.

[51] T. Hou, K.D. Fong, J. Wang, and K.A. Persson. The solvation structure, transport properties and reduction behavior of carbonate-based electrolytes of lithium-ion batteries. *Chem. Sci.*, 12:14740–14751, 2021.

[52] L. Benitez, D. Cristancho, J.M. Seminario, J.M. Martinez de la Hoz, and P.B. Balbuena. Electron transfer through solid-electrolyte-interphase layers formed on Si anodes of Li-ion batteries. *Electrochim. Acta*, 140:250–257, 2014.

[53] J.M. Martínez de la Hoz and P.B. Balbuena. Reduction mechanisms of additives on Si anodes of Li-ion batteries. *Phys. Chem. Chem. Phys.*, 16(32):17091–17098, 2014.

[54] L. Alzate-Vargas, S.M. Blau, E.W.C. Spotte-Smith, S. Allu, K.A. Persson, and J.-L. Fattebert. Insight into SEI growth in Li-ion batteries using molecular dynamics and accelerated chemical reactions. *J. Phys. Chem. C*, 125(34):18588–18596, 2021.

[55] E.M. Gavilán-Arriazu, M.P. Mercer, D.E. Barraco, H.E. Hoster, and E.P.M. Leiva. Kinetic Monte Carlo simulations applied to Li-ion and post Li-ion batteries: a key link in the multi-scale chain. *Progress in Energy*, 3(4):042001, 2021.

[56] R.N. Methekar, P.W.C. Northrop, K. Chen, R.D. Braatz, and V.R. Subramanian. Kinetic Monte Carlo simulation of surface heterogeneity in graphite anodes for lithium-ion batteries: passive layer formation. *J. Electrochem. Soc.*, 158(4):A363, 2011.

[57] F. Röder, R.D. Braatz, and U. Krewer. Multi-scale simulation of heterogeneous surface film growth mechansisms in lithium-ion batteries. *J. Electrochem. Soc.*, 164:E3335–E3344, 2017.

[58] D. Aurbach and A. Zaban. Impedance spectroscopy of lithium electrodes: Part 1. General behavior in propylene carbonate solutions and the correlation to surface chemistry and cycling efficiency. *J. Electroanal. Chem.*, 348:155–179, 1993.

[59] E. Peled, D. Golodnitsky, and G. Ardel. Advanced model for solid electrolyte interphase electrodes in liquid and polymer electrolytes. *J. Electrochem. Soc.*, 144(8):L208–L210, 1997.

[60] M. Uppaluri, K. Shah, V. Viswanathan, and V.R. Subramanian. The importance of a moving boundary approach for modeling the SEI layer growth to predict capacity fade. *J. Electrochem. Soc.*, 169:040548, 2022.

[61] J. Christensen and J. Newman. A mathematical model for the lithium-ion negative electrode solid electrolyte interphase. *J. Electrochem. Soc.*, 151:A1977–A1988, 2004.

[62] C. Kupper and W.G. Bessler. Multi-scale thermo-electrochemical modeling of performance and aging of a LiFePO$_4$/graphite lithium-ion cell. *J. Electrochem. Soc.*, 164(2):A304–A320, 2017.

[63] C. Shinagawa, H. Ushiyama, and K. Yamashita. Multiscale simulations for lithium-ion batteries: SEI film growth and capacity fading. *J. Electrochem. Soc.*, 164:A3018, 2017.

[64] D. Witt, F. Röder, and U. Krewer. Analysis of lithium-ion battery state and degradation via physicochemical cell and SEI modeling. *Batt. Supercaps*, 2022.

[65] M. Safari, M. Morcrette, A. Teyssot, and C. Delacourt. Multi-modal physics-based aging model for life prediction of Li-ion batteries. *J. Electrochem. Soc.*, 156:A145–A153, 2009.

[66] R. Li, S. O'Kane, M. Marinescu, and G.J. Offer. Modelling solvent consumption from SEI growth in lithium-ion batteries. *J. Electrochem. Soc.*, 169:060516, 2022.

[67] V. Sulzer, P. Mohtat, S. Pannala, J.B. Siegel, and A.G. Stefanopoulou. Accelerated battery lifetime simuations using adaptive inter-cycle extrapolation. *J. Electrochem. Soc.*, 168:120531, 2021.

[68] F. Röder, V. Laue, and U. Krewer. Model based muliscale analysis of film formation in lithium-ion batteries. *Batt. Supercaps*, 2:248–265, 2019.

[69] F. Single, B. Horstmann, and A. Latz. Revealing SEI morphology: In depth analysis of modeling approach. *J. Electrochem. Soc.*, pages E3132–E3145, 2017.

[70] D. Korff, A.M. Colclasure, Y. Ha, K.A. Smith, and S.C. DeCaluwe. Pathways toward high-energy Li-sulfur batteries, identified via multi-reaction chemical modeling. *J. Electrochem. Soc.*, 169:010520, 2022.

[71] M. Gerasimov, F.A. Soto, J. Wagner, F. Baakes, N. Guo, F. Ospina-Acevedo, F. Röder, P.B. Balbuena, and U. Krewer. Species distribution during solid electrolyte interphase formation on lithium using MD/DFT-parameterized kinetic Monte Carlo simulations. *J. Phys. Chem. C*, 127:4872–4886, 2023.

[72] S.C. DeCaluwe, P.J. Weddle, H. Zhu, A.M. Colclasure, W.G. Bessler, G.S. Jackson, and R.J. Kee. On the fundamental and practical aspects of modeling complex electrochemical kinetics and transport. *J. Electrochem. Soc.*, pages E637–E658, 2018.

[73] F. Bierbrauer. Hydrogel drug delivery: diffusion models. Technical report, School of Mathematics & Applied Statistics, University of Wollongong, 2005.

[74] P. Löstedt and L. Petzold. Numerical solution of nonlinear differential equations with algebraic constraints I. Converge results for backward differentiation formulas. *Math. Comput.*, 46:491–516, 1986.

[75] R.J. Kee, M.E. Coltrin, P. Glarborg, and H. Zhu. *Chemically reacting flow: Theory, modeling and simulation*. Wiley, Hoboken, NJ, 2nd edition, 2018.

[76] S.M. Mahali, A. Setapa, and N.N. Zolkamal. Mathematical model for drug release from a logistically swelling hydrogel. *AIP Conference Proceedings*, page 020068, 1974.

[77] J. Newman and K.E. Thomas-Alyea. *Electrochemical systems*. Wiley, Hoboken, NJ, 2004.

[78] N.R. Shaffer, S.D. Baalrud, and J. Daligault. Effective potential theory for diffusion in binary ionic mixtures. *Phys. Rev. E*, 95:013206, 2017.

[79] T.S. Thacher, J.-L. Lin, and C.Y. Mou. Theory of Onsager phenomenological coefficients for isothermal linear transport processes in electrolyte solutions. *J. Chem. Phys.*, 2053:81, 1984.

[80] J.-F. Dufrêche, O. Bernard, S. Durand-Vidal, and P. Turq. Analytical theories of transport in concentrated electrolyte solutions from the MSA. *J. Phys. Chem.*, 109:9873–9884, 2005.

[81] J.O. Hirschfelder, C.F. Curtiss, and R.B. Bird. *Molecular the-*

ory of fases and liquids. John Wiley & Sons Ltd, 1954.

[82] A.A. Franco, A. Rucci, D. Brandell, C. Frayret, M. Gaberscek, P. Jankowski, and P. Johansson. Boosting rechargable batteries R&D by multiscale modeling: Myth or Reality. *Chem. Rev.*, 119(7):4569–4627, 2019.

[83] M.D. Bhatt, M. Cho, and K. Cho. Density functional theory calculations and ab initio molecular dynamics simulations for diffusion of Li$^+$ within liquid ethylene carbonate. *Model. Simul. Mater. Sci. Eng.*, 20:065004, 2012.

[84] A. Ehrl, J. Landesfeind, W.A. Wall, and H.A. Gasteiger. Determination of transport parameters in liquid binary lithium ion battery electrolytes: Part I. Diffusion coefficient. *J. Electrochem. Soc.*, 164:A826–A836, 2017.

[85] A. Ehrl, J. Landsfiend, W.A. Wall, and H.A. Gasteiger. Determination of transport parameters in liquid binary lithium ion battery electrolytes: Part II. Transference number. *J. Electrochem. Soc.*, 164:A2716–A2731, 2017.

[86] D.G. Goodwin, H.K. Moffat, and R.L. Speth. Cantera: An object-oriented software toolkit for chemical kinetics, thermodynamics, and transport processes, 2017. Version 2.3.0.

[87] S.C. DeCaluwe. Open software for chemical and electrochemical modeling: Opprotunities and challenges. *Electrochem. Soc. Interface*, 28(47):47–50, 2019.

[88] T. Hou, G. Yang, N.N. Rajput, J. Self, S.-W. Park, J. Nanda, and K.A. Persson. The influence of FEC on the solvation structure and reduction reaction of LiPF$_6$/EC electrolytes and its implication for solid electrolyte interphase formation. *Nano Energy*, 64:103881, 2019.

[89] E. Epifanovsky et al. Software for the frontiers of quantum chemistry: An overview of developments in the Q-Chem 5 package. *J. Chem. Phys.*, 155:084801, 2021.

[90] N. Mardirossian and M. Head-Gordon. ωB97X-V: A 10-parameter, range-separated hybrid, generalized gradient approximation density functional with nonlocal correlation, designed by a survival-of-the-fittest strategy. *Phys. Chem. Chem. Phys.*, 16:9904–9924, 2014.

[91] D. Rappoport and F. Furche. Property-optimized Gaussian basis sets for molecular response calculations. *J. Chem. Phys.*, 133(13):134105, 2010.

[92] A.V. Marenich, C.J. Cramer, and D.G. Trahlar. Universal solvation model based on solute electron density and on a continuum model of the solvent defined by the bulk dielectric constant and atomic surface tensions. *J. Phys. Chem.*, 113(8):6378–6396, 2009.

[93] E.W.C. Spotte-Smith, S.M. Blau, X. Xie, H.D. Patel, M. Wen, B. Wood, S. Dwaraknath, and K.A. Persson. Quantum chemical calculations of lithium-ion battery electrolyte and interphase species. *Sci. Data*, 8:203, 2021.

[94] E. Arca, G.M. Veith, R. Satish, T. Lin, G. Teeter, and R. Kostecki. Understanding the origin of nonpassivating behavior of Si-based anodes during initial cycles. *J. Phys. Chem. C*, 126:14058–14066, 2022.

[95] K. Xu. Whether EC and PC differ in interphasial chemistry on graphitic anode and how. *J. Electrochem. Soc.*, 156:A751, 2009.

[96] K. Leung, F. Soto, K. Hankins, P.B. Balbuena, and K.L. Harrison. Stability of solid electrolyte interphase components on lithium metal and reactive anode material surfaces. *J. Phys. Chem. C*, 12:6302–6313, 2016.

[97] K. Tasaki and S.J. Harris. Computational study on the solubility of lithium salts formed on lithium ion battery negative electrode in organic solvents. *J. Phys. Chem. C*, 114:8076–8083, 2010.

[98] K. Ushirogata, K. Sodeyama, Z. Futera, Y. Tateyama, and Y. Okuno. Near-shore aggregation mechanism of electrolyte

decomposition products to explain solid electrolyte interface formation. *J. Electrochem. Soc.*, 162:A2670, 2015.

[99] L. Cheng, R. Redfern, K.C. Lau, R.S. Assary, B. Narayanan, and L.A. Curtiss. Computational studies of solubilities of LiO$_2$ and Li$_2$O$_2$ in aprotic solvents. *J. Electrochem. Soc.*, 11:E3696–E3701, 2017.

[100] L.D. Jacobson, A.D. Bochevarov, M.A. Watson, T.F. Hughes, D. Rinaldo, S. Ehrlich, T.B. Steinbrecher, S. Vaitheeswaran, D.M. Philipp, M.D. Halls, and R.A. Friesner. Automated transition state search and its application to diverse types of organic reactions. *J. Chem. Theory Comput.*, 13(11):5780–5797, 2017.

[101] A.D. Bochevarov, E. Harder, T.F. Hughes, J.R. Greenwoodand D.A. Braden, D.M. Philipp, D. Rinaldo, M.D. Halls, J. Zhang, and R.A. Friesner. Jaguar: A high-performance quantum chemistry software program with strengths in life and materials sciences. *Int. J. Quantum Chem.*, 113:2110–2142, 2013.

[102] J.-D. Chai and M. Head-Gordon. Long-range corrected hybrid density functionals with damped atom–atom dispersion corrections. *Phys. Chem. Chem. Phys.*, 10:6615–6620, 2008.

[103] Benedetta Mennucci. Polarizable continuum model. *Wiley Interdiscip. Rev. Comput. Mol. Sci.*, 2(3):386–404, 2012.

[104] T. Yoon, M.S. Milien, B.S. Parimalam, and B.L. Lucht. Thermal decomposition of the solid electrolyte interphase (SEI) on silicon electrodes for lithium ion batteries. *Chem. Mater.*, 29:3237–3245, 2017.

[105] R.A. Marcus. Electron transfer reactions in chemistry: theory and experiment (Nobel lecture). *Angew. Chem., Int. Ed. Engl.*, 32(8):1111–1121, 1993.

[106] S.F. Nelsen, S.C. Blackstock, and Y. Kim. Estimation of inner shell Marcus terms for amino nitrogen compounds by molecular orbital calculations. *J. Am. Chem. Soc.*, 109(3):677–682, 1987.

[107] Y. Jin, N.-J. H. Kneusels, L.E. Marbella, E. Castillo-Martínez, P.C.M.M. Magusin, R.S. Weatherup, E. Jónsson, T. Liu, S. Paul, and C.P. Grey. Understanding fluoroethylene carbonate and vinylene carbonate based electrolytes for Si anodes in lithium ion batteries with NMR spectroscopy. *J. Am. Chem. Soc.*, 140:9854–9867, 2018.

[108] Y. Jin, N.-J.H. Kneusels, P.C.M.M. Magusin, G. Kim, E. Castillo-Martínez, L.E. Marbella, R.N. Kerber, D.J. Howe, S. Paul, T. Liu, and C.P. Grey. Identifying the structural basis for the increased stability of the solid electrolyte interphase formed on silicon with the additive fluoroethylene carbonate. *J. Am. Chem. Soc.*, 139:14992–15004, 2017.

[109] A.L. Michan, B.S. Parimalam, M. Leskes, R.N. Kerber, T. Yoon, C.P. Grey, and B.L. Lucht. Fluoroethylene carbonate and vinylene carbonate reduction: Understanding lithium-ion battery electrolyte additives and solid electrolyte interphase formation. *Chem. Mater.*, 28:8149–8159, 2016.

[110] I.A. Shkrob, J.F. Wishart, and D.P. Abraham. What makes fluoroethylene carbonate different? *J. Phys. Chem. C*, 119:14954–14964, 2015.

[111] V. Etacheri, O. Haik, Y. Goffer, G.A. Roberts, I.C. Stefan, R. Fasching, and D. Aurbach. Effect of fluoroethylene carbonate (FEC) on the performance and surface chemistry of Si-nanowire Li-ion battery anodes. *Langmuir*, 28 (1):965–976, 2012.

[112] X. Zhao, Q.-C. Zhuang, S.-D. Xu, Y.-X. Xu, Y.-L. Shi, and X.-X. Zhang. A new insight into the content effect of fluoroethylene carbonate as a film forming additive for lithium-ion batteries. *Int. J. Electrochem. Sci.*, 10:2515–2534, 2015.

[113] I.A. Shkrob, Y. Zhu, T.W. Marin, and D. Abraham. Reduction of carbonate electrolytes and the formation of solid-electrolyte interface (SEI) in lithium-ion batteries. 1. Spectroscopic ob-

servations of radical intermediates generated in one-electron reduction of carbonates. *J. Phys. Chem. C*, 117:19255–19269, 2013.

[114] I.A. Shkrob, Y. Zhu, T.W. Marin, and D. Abraham. Reduction of carbonate electrolytes and the formation of solid-electrolyte interface (SEI) in lithium-ion batteries. 2. Radiolytically induced polymerization of ethylene carbonate. *J. Phys. Chem. C*, 117:19270–19279, 2013.

[115] L. Bläubaum, P. Röse, and U. Krewer. The effects of gas saturation of electrolytes on the performance and durability of lithium-ion batteries. *ChemSusChem*, 14:2943–2951, 2021.

[116] R. Petibon, L. Rotermund, K.J. Nelson, A.S. Gozdz, J. Xia, and J.R. Dahn. Study of electrolyte components in Li ion cells using liquid-liquid extraction and gas chromatography coupled with mass spectrometry. *J. Electrochem. Soc.*, 161:A1167–A1172, 2014.

[117] R. Petibon, V.L. Chevrier, C.P. Aiken, D.S. Hall, S.R. Hyatt, R. Shunmugasundaram, and J.R. Dahn. Studies of the capacity fade mechanisms of LiCoO$_2$/Si-alloy: Graphite cells. *J. Electrochem. Soc.*, 163:A1146–A1156, 2016.

[118] B. Strehle, S. Solchenbach, M. Metzger, K.U. Schwenke, and H.A. Gasteiger. The effect of CO$_2$ on alkyl carbonate trans-esterification during formation of graphite electrodes in Li-ion batteries. *J. Electrochem. Soc.*, 164:A2513, 2017.

[119] C. Peschel, F. Horsthemke, M. Leißing, S. Wiemers-Meyer, J. Henschel, L. Ibing, M. Winter, and S. Nowak. Analysis of carbonate decomposition during solid electrolyte interphase formation in isotope-labeled lithium ion battery electrolytes: Extending the knowledge about electrolyte soluble species. *Batter. Supercaps*, 3:1183–1192, 2020.

[120] Y. Ha, C. Stetson, S.P. Harvey, G. Teeter, B.J. Tremolet de Villers, C.-S. Jiang, C. Schnabel, P. Stradins, A. Burrell, and S.-D. Han. Effect of water concentration in LiPF$_6$-based electrolytes on the formation, evolution, and properties of solid electrolyte interphases on Si anodes. *Appl. Mater. Interfaces*, 12:49563–49573, 2020.

[121] Y. He, L. Jiang, T. Chen, Y. Xu, H. Jia, R. Yi, D. Xue, M. Song, A. Genc, C. Bouchet-Marquis, L. Pullan, T. Tessner, J. Yoo, X. Li, J.-G. Zhang, S. Zhang, and C. Wang. Progressive growth of the solid-electrolyte interface towards the Si anode interior causes capacity fade. *Nature Nanotechnol.*, 16:1113–1120, 2021.

[122] D. Aurbach. Review of selected electrode-solution interactions which determine the performance of Li and Li ion batteries. *J. Power Sources*, 89:206–218, 2000.

[123] X. Su, Q. Wu, J. Li, X. Xiao, A. Lott, W. Lu, B.W. Sheldon, and J. Wu. Silicon-based nanomaterials for lithium-ion batteries: A review. *Adv. Energy Mater.*, 4:1300882, 2014.

[124] W. Mai, A.M. Colclasure, and K. Smith. A reformulation of the Pseudo2D battery model coupling large electrochemical-mechanical deformations at particle and electrode levels. *J. Electrochem. Soc.*, 166:A1330–A1339, 2019.

[125] M. Tanaka, J.B. Hooper, and D. Bedrov. Role of plasticity in mechanical failure of solid electrolyte interphases on nanostructured silicon eletrode: Insight from continuum level modeling. *ACS Appl. Energy Mater.*, 1(5):1858–1863, 2018.

[126] P. Ganesh, P.R.C. Kent, and D. Jiang. Solid-electrolyte interphase formation and electrolyte reduction at Li-ion battery graphite anodes: Insights from first-principles molecular dynamics. *J. Phys. Chem. C*, 116(46):24476–24481, 2012.

[127] C.L. Seitzinger, R.L. Sacci, J.E. Coyle, C.A. Apblett, K.A. Hays, R.R. Armstrong, A.M. Rogers, B.L. Armstrong, T.H. Bennet, N.R. Neale, and G.M. Veith. Intrinsic chemical reactivity of silicon electrode materials: Gas evolution. *Chem. Mater.*, 32:3199–3210, 2020.

[128] X. Zhang, D. Wang, X. Qiu, Y. Ma, D. Kong, K. Müllen, X. Li, and L. Zhi. Stable high-capacity and high-rate silicon-based lithium battery anodes upon two-dimensional covalent encapsulation. *Nat. Commun.*, 11:3826, 2020.

[129] J. Yu, P.B. Balbuena, J. Budzien, and K. Leung. Hybrid DFT functional-based static and molecular dynamics studies of excess electron in liquid ethylene carbonate. *J. Electrochem. Soc.*, 158(4):A400–A410, 2011.

[130] M. Leißing, C. Peschel, F. Horsthemke, S. Wiemers-Meyer, M. Winter, and S. Nowak. The origin of gaseous decomposition products formed during SEI formation analyzed by isotope labeling in lithium-ion battery electrolytes. *Batter. Supercaps*, 4:1731–1738, 2021.

[131] C. Stetson, T. Yoon, J. Coyle, W. Nemeth, M. Young, A. Norman, S. Pylypenko, C. Ban, C.-S. Jiang, M. Al-Jassim, and A. Burrell. Three-dimensional electronic resistivity mapping of solid electrolyte interphase on Si anodes materials. *Nano Energy*, 55:477–485, 2019.

[132] K.N. Wood and G. Teeter. XPS on Li-battery-related componds: Analysis of inorganic SEI phases and a methodology for charge correction. *Appl. Energy Mater.*, 1:4493–4504, 2018.

[133] G.M. Veith, M. Doucet, J.K. Baldwin, R.L. Sacci, T.M. Fears, Y. Wang, and J.F. Browning. Direct determination of solid-electrolyte interphase thickness and composition as a function of state of charge on a silicon anode. *J. Phys. Chem. C*, 119:20339–20349, 2015.

[134] T. Liu, L. Lin, X. Bi, L. Tian, K. Yang, J. Liu, M. Li, Z. Chen, J. Lu, K. Amine, K. Xu, and F. Pan. In situ quantification of interphasial chemistry in Li-ion battery. *Nat. Nanotechnol.*, 14:50–56, 2019.

[135] T. Kohler, E. Hadjixenophontos, Y. Joshi, K. Wang, and G. Schmitx. Reversible oxide formation during cycling of Si anodes. *Nano Energy*, 84:105886, 2021.

[136] D.M. Seo, D. Chalasani, B.S. Parimalam, R. Kadam, M. Nie, and B.L. Lucht. Reduction reactions of carbonate solvents for lithium ion batteries. *ECS Electrochem. Lett.*, 3:A91, 2014.

[137] E.J. Hopkins, S. Frisco, R.T. Pekarek, C. Stetson, Z. Huey, S. Harvey, X. Li, B. Key, C. Fang, G. Liu, G. Yang, G. Teeter, N.R. Neale, and G.M. Veith. Examining CO$_2$ as an additive for solid electrolyte interphase formation on silicon anodes. *J. Electrochem. Soc.*, 168:030534, 2021.

[138] F. La Mantia and P. Novák. Online detection of reductive CO$_2$ development at graphite electrodes in the 1 M LiPF$_6$, EC:DMC battery electrolyte. *Electrochem. Solid-State Lett.*, 11:A84, 2008.

[139] Y.R. Dougassa, C. Tessier, L. El Ouatani, M. Anouti, and J. Jacquemin. Low pressure carbon dioxide solubility in lithium-ion batteries based electrolytes as a function of temperature. Measurement and prediction. *J. Chem. Thermodyn.*, 61:32–44, 2013.

[140] Y.R. Dougassa, J. Jacquemin, L. El Ouatani, C. Tessier, and M. Anouti. Viscosity and carbon dioxide solubility for LiPF$_6$, LiTFSI, and LiFAP in alkyl carbonates: Lithium salt nature and concentration effects. *J. Phys. Chem. B*, 118:3973–3980, 2014.

[141] E. Bahzadfar and S.G. Hatzikiriakos. Diffusivity of CO$_2$ in bitumen: Pressure–decay measurements coupled with rheometry. *Energy Fuels*, 28:1304–1311, 2014.

[142] W. Huang, J. Wang, M.R. Braun, Z. Zhang, Y. Li, D.T. Boyle, P.C. McIntyre, and Y. Cui. Dynamic structure and chemistry of the silicon solid-electrolyte interphase visualized by cryogenic electron microscopy. *Matter*, 1:1232–1245, 2019.

Supplemental Material

S1. Mechanism inputs

Table S1 documents observations of common SEI species reported in the literature and their reported solubility. Table S2 documents the heterogeneous reduction reactions and the deposition/dissolution reactions at the SEI/electrolyte interface. Table S3 and Table S4 document the homogeneous electrolyte reactions considered in the model.

Table S1: Common SEI species measured/predicted in the literature

Species	Notes
LEDC	Expected to deposit/dissolve without forming new solid-phase products [15]. This is contradictory to the simplified mechanism proposed by Single [69]. There is contradictory literature on species solubility. Some say that LEDC has quite low solubility [95], while others say it is quite high [97]. This is expected to be a primary SEI component [96].
Li_2CO_3	Expected to form in the outer SEI (of Li metal) [122]. This species is proposed for many mechanisms and is a primary SEI component [9, 96].
LiF	Expected to form quickly (i.e., the inner layer) if FEC is in the electrolyte [122].
Li_2O	Expected to form in the inner SEI (of Li metal) [122]. May be due to solid-phase conversion of Li_2EDC and Li_2CO_3 [69, 96]. Expected to be a primary SEI component [142]. However, measurements show that upon delithiation, Li_2O is no longer in the SEI. Either it reacts with the Si to form Li_xSiO_y or it dissolves [142]. May result from FEC reacting with Li_2CO_3 [45].
LiOH	Expected to form in the outer SEI (of Li metal) [122].

Table S2: Heterogeneous reactions

Reaction number	Reaction	Forward rate constant k_{fs} (kmol, m, s) at 100 mV	Reorganization energy λ/eV	Equilibrium voltage E^{eq}/V
R1	LiEC$^+_{el}$ + e$^-_{SEI}$ ⇌ LiEC$_{el}$	1.649E+00	1.933E+00	0.810
R2	LiEC$_{el}$ + e$^-_{SEI}$ ⇌ LiEC$^-_{el}$	8.545E-02	1.623E+00	0.409
R3	LiEC_RO$_{el}$ + e$^-_{SEI}$ ⇌ LiEC_RO$^-_{el}$	5.081E+03	1.409E+00	1.537
R4	LiDMC$^+_{el}$ + e$^-_{SEI}$ ⇌ LiDMC$_{el}$	8.906E-01	1.816E+00	0.686
R5	LiEMC$^+_{el}$ + e$^-_{SEI}$ ⇌ LiEMC$_{el}$	7.215E-01	1.805E+00	0.663
R6	LiDEC$^+_{el}$ + e$^-_{SEI}$ ⇌ LiDEC$_{el}$	5.673E-01	1.795E+00	0.640
R7	LiFEC$^+_{el}$ + e$^-_{SEI}$ ⇌ LiFEC$_{el}$	3.096E+00	2.151E+00	1.012
R8	LiVC$^+_{el}$ + e$^-_{SEI}$ ⇌ LiVC$_{el}$	2.969E+00	2.007E+00	0.908
R9	LiVC_RO$_{el}$ + e$^-_{SEI}$ ⇌ LiVC_RO$^-_{el}$	3.005E+01	1.379E+00	2.373
R10	LiCH$_3$OCO$^+_{el}$ + e$^-_{SEI}$ ⇌ LiCH$_3$OCO$_{el}$	4.119E-02	1.835E+00	3.462
R11	LiCH$_3$CH$_2$OCO$^+_{el}$ + e$^-_{SEI}$ ⇌ LiCH$_3$CH$_2$OCO$_{el}$	7.322E-02	1.834E+00	3.424
R12	FEC_RO_lessLiF$_{el}$ + e$^-_{SEI}$ ⇌ FEC_RO_lessLiF$^-_{el}$	2.949E+02	1.554E+00	2.369
R13	LiPC$^+_{el}$ + e$^-_{SEI}$ ⇌ LiPC$_{el}$	2.363E-01	1.904E+00	0.647
R14	LiPC_RO$_{el}$ + e$^-_{SEI}$ ⇌ C$_3$H$_{6el}$ + LiCO$_3^-{}_{el}$	6.019E+02	1.437E+00	20.862
R15	LiBC$^+_{el}$ + e$^-_{SEI}$ ⇌ LiBC$_{el}$	1.260E+03	8.169E-01	0.615
R16	LiBC_RO$_{el}$ + e$^-_{SEI}$ ⇌ C$_4$H$_{8el}$ + LiCO$_3^-{}_{el}$	7.044E+02	1.365E+00	20.861
R17	LiFEC_lessH$^+_{el}$ + e$^-_{SEI}$ ⇌ LiF$_{el}$ + VC$_{el}$	4.540E+03	2.451E+00	22.573
R18	Li$_2$CO$_{3el}$ ⇌ Li$_2$CO$_{3SEI}$	6.212E-02[†]	–	–
R19	LEDC$_{el}$ ⇌ LEDC$_{SEI}$	6.212E-02[†]	–	–
R20	LiF$_{el}$ ⇌ LiF$_{SEI}$	6.212E-02[†]	–	–
R21	LMC$_{el}$ ⇌ LMC$_{SEI}$	6.212E-02[†]	–	–
R22	LEC$_{el}$ ⇌ LEC$_{SEI}$	6.212E-02[†]	–	–

[†] Assumed

Table S3: Homogeneous reactions in the electrolyte (not including metal hopping reactions)[†]

Reaction number	Reaction	Forward rate constant k_f (m, s, kmol)
EC decomposition		
H1	$EC_{el} + Li^+_{el} \rightleftharpoons LiEC^+_{el}$	6.212E+12
H2	$LiEC_{el} \rightleftharpoons LiEC\_RO_{el}$	1.076E+06
H3	$LiEC\_RO_{el} + LiEC\_RO_{el} \rightleftharpoons LEDC_{el} + C_2H_{4el}$	6.212E+12
H4	$LiEC\_RO^-_{el} \rightleftharpoons C_2H_{4el} + LiCO^-_{3el}$	3.942E+10
H5	$LiCO^-_{3el} + Li^+_{el} \rightleftharpoons Li_2CO^-_{3el}$	6.212E+12
H6	$LiCO^-_{3el} + LiEC^+_{el} \rightleftharpoons LEDC_{el}$	2.421E+07
H7	$LiEC^-_{el} \rightleftharpoons LiEC\_RO\_shoulder_{el}$	4.377E+12
H8	$LiEC\_RO\_shoulder_{el} \rightleftharpoons CO_{el} + Li(OCH_2)^-_{2el}$	4.377E+12
H9	$Li(OCH_2)^-_{2el} + CO_{2el} + CO_{2el} \rightleftharpoons LEDC\_lessLi_{el}$	6.212E+12
H10	$LEDC\_lessLi_{el} + Li^+_{el} \rightleftharpoons LEDC_{el}$	6.212E+12
H11	$Li(OCH_2)^-_{2el} + LiEC^+_{el} \rightleftharpoons PEC\_PEO\_dimer_{el}$	1.695E+08
H12	$Li(OCH_2)^-_{2el} + EC_{el} \rightleftharpoons PEC\_dimer\_closed_{el}$	6.828E+03
H13	$PEC\_dimer\_closed_{el} \rightleftharpoons PEC\_dimer\_open\_Li_{el}$	5.317E+12
DMC decomposition		
H14	$DMC_{el} + Li^+_{el} \rightleftharpoons LiDMC^+_{el}$	6.212E+12
H15	$LiDMC_{el} \rightleftharpoons LMC_{el} + CH_{3el}$	4.780E+04
H16	$LiDMC_{el} \rightleftharpoons LiOCH_{3el} + CH_3OCO_{el}$	2.124E+03
H17	$CH_{3el} + CH_{3el} \rightleftharpoons C_2H_{6el}$	6.212E+12
H18	$CH_{3el} + EC_{el} \rightleftharpoons CH_{4el} + EC\_lessH_{el}$	5.609E-03
H19	$CH_{3el} + EC\_lessH_{el} \rightleftharpoons PC_{el}$	6.212E+12
H20	$CH_{3el} + EC\_lessH_{el} \rightleftharpoons CH_{4el} + VC_{el}$	6.212E+12
H21	$CH_{3el} + FEC_{el} \rightleftharpoons CH_{4el} + FEC\_lessH_{el}$	6.828E+03
H22	$FEC\_lessH_{el} + Li^+_{el} \rightleftharpoons LiFEC\_lessH^+_{el}$	6.212E+12
EMC decomposition		
H23	$EMC_{el} + Li^+_{el} \rightleftharpoons LiEMC^+_{el}$	6.212E+12
H24	$LiEMC_{el} \rightleftharpoons LEC_{el} + CH_{3el}$	4.333E+01
H25	$LiEMC_{el} \rightleftharpoons LMC_{el} + C_2H_{5el}$	9.133E+00
H26	$LiEMC_{el} \rightleftharpoons LiOCH_{3el} + CH_3CH_2OCO_{el}$	2.268E+05
H27	$LiEMC_{el} \rightleftharpoons LiOCH_2CH_{3el} + CH_3OCO_{el}$	4.780E+04
H28	$CH_{3el} + C_2H_{5el} \rightleftharpoons C_3H_{8el}$	6.212E+12
H29	$C_2H_{5el} + EC_{el} \rightleftharpoons C_2H_{6el} + EC\_lessH_{el}$	9.752E+02
H30	$C_2H_{5el} + FEC_{el} \rightleftharpoons C_2H_{6el} + FEC\_lessH_{el}$	9.752E+02
H31	$C_2H_{5el} + EC\_lessH_{el} \rightleftharpoons C_2H_{6el} + VC_{el}$	6.212E+12
H32	$C_2H_{5el} + EC\_lessH_{el} \rightleftharpoons BC_{el}$	6.212E+12
Transesterification		
H33	$CH_3OCO_{el} + Li^+_{el} \rightleftharpoons LiCH_3OCO^+_{el}$	6.212E+12
H34	$CH_3CH_2OCO_{el} + Li^+_{el} \rightleftharpoons LiCH_3CH_2OCO^+_{el}$	6.212E+12
H35	$LiCH_3OCO_{el} \rightleftharpoons CO_{el} + LiOCH_{3el}$	4.377E+12
H36	$LiCH_3CH_2OCO_{el} \rightleftharpoons CO_{el} + LiOCH_2CH_{3el}$	8.587E+10
H37	$LiCH_3OCO_{el} + EMC_{el} \rightleftharpoons LiTetra_{112el}$	1.076E+06
H38	$LiCH_3CH_2OCO_{el} + EMC_{el} \rightleftharpoons LiTetra_{122el}$	1.588E+06
H39	$LiTetra_{112el} \rightleftharpoons LiCH_3CH_2OCO_{el} + DMC_{el}$	4.377E+12
H40	$LiTetra_{122el} \rightleftharpoons LiCH_3OCO_{el} + DEC_{el}$	5.317E+12
DEC decomposition		
H41	$DEC_{el} + Li^+_{el} \rightleftharpoons LiDEC^+_{el}$	6.212E+12
H42	$LiDEC_{el} \rightleftharpoons LEC_{el} + C_2H_{5el}$	9.133E+00
H43	$LiDEC_{el} \rightleftharpoons LiOCH_2CH_{3el} + CH_3CH_2OCO_{el}$	4.939E+05
FEC decomposition		
H44	$FEC_{el} + Li^+_{el} \rightleftharpoons LiFEC^+_{el}$	6.212E+12
H45	$LiFEC_{el} \rightleftharpoons LiFEC\_RO_{el}$	4.377E+12
H46	$LiFEC\_RO_{el} \rightleftharpoons LiF_{el} + FEC\_RO\_lessLiF_{el}$	4.377E+12
H47	$FEC\_RO\_lessLiF^-_{el} + FEC_{el} \rightleftharpoons CO_{2el} + FEC\_dimer^-_{el}$	5.989E-01
FEC & Transesterification intermediates		
H48	$LiOCH_{3el} + FEC_{el} \rightleftharpoons methoxydioxolanone_{el} + LiF_{el}$	1.187E+09
H49	$LiOCH_2CH_{3el} + FEC_{el} \rightleftharpoons ethoxydioxolanone_{el}$	2.671E+10
H50	$LiOCH_{3el} + FEC_{el} \rightleftharpoons moec_{el} + LiF_{el}$	2.585E+09
H51	$LiOCH_2CH_{3el} + FEC_{el} \rightleftharpoons eoec_{el} + LiF_{el}$	1.187E+09
VC decomposition		
H52	$VC_{el} + Li^+_{el} \rightleftharpoons LiVC^+_{el}$	6.212E+12
H53	$LiVC_{el} \rightleftharpoons LiVC\_RO_{el}$	8.873E+11
H54	$LiVC\_RO^-_{el} \rightleftharpoons C_2H_{2el} + LiCO^-_{3el}$	1.588E+06
PC decomposition		
H55	$PC_{el} + Li^+_{el} \rightleftharpoons LiPC^+_{el}$	6.212E+12
H56	$LiPC_{el} \rightleftharpoons LiPC\_RO_{el}$	5.274E+07
BC decomposition		
H57	$BC_{el} + Li^+_{el} \rightleftharpoons LiBC^+_{el}$	6.212E+12
H58	$LiBC_{el} \rightleftharpoons LiBC\_RO_{el}$	5.274E+07
Other reactions		
H59	$CO_{2el} + Li^+_{el} \rightleftharpoons LiCO^+_{2el}$	6.212E+12

[†] Reactions are organized into sections that correspond to groupings in Fig. 2

3

Table S4: Homogeneous metal hopping reactions in the electrolyte

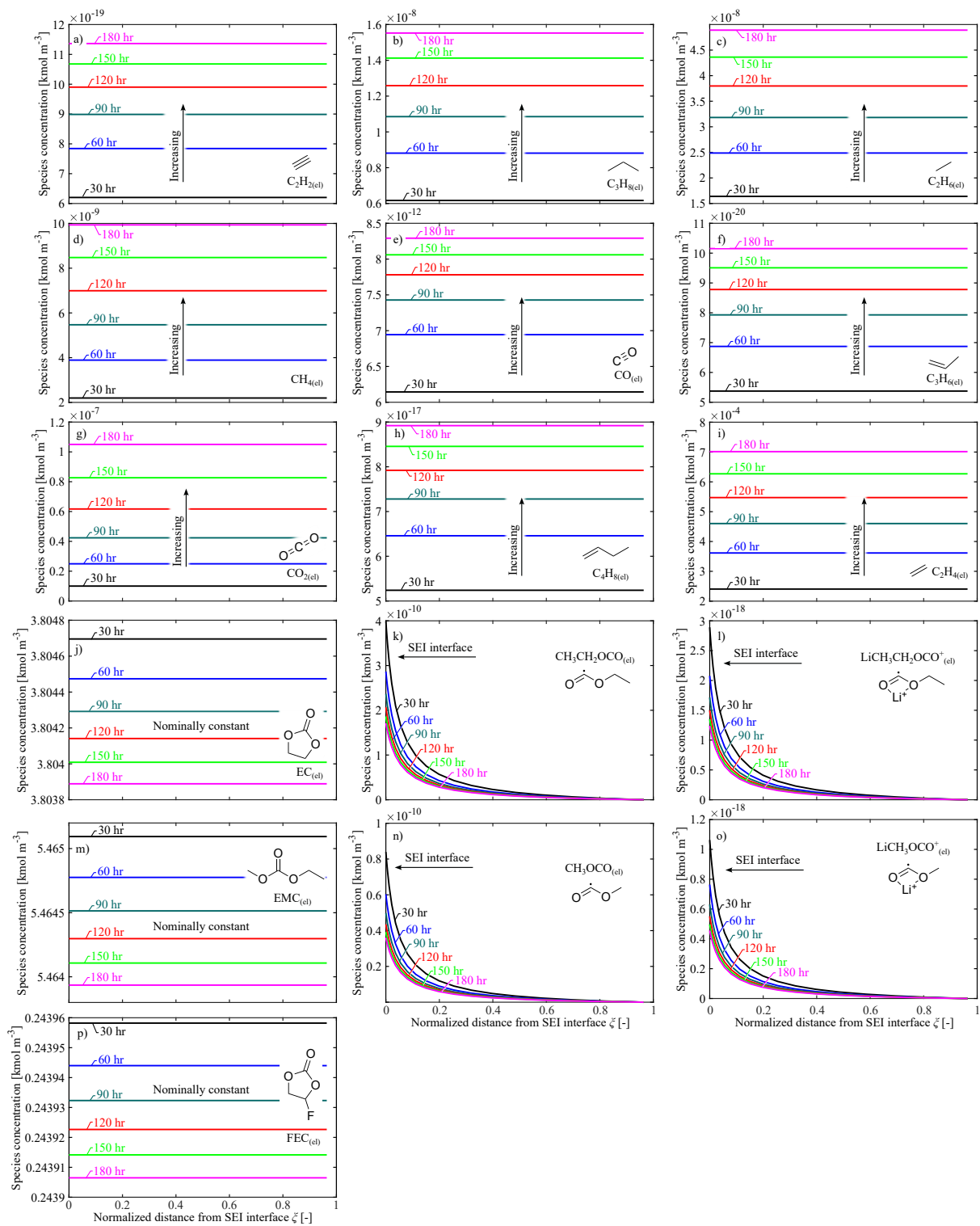| Reaction number	Reaction	Forward rate constant k_f (m, s, kmol)[†]
H60	$EC_{el} + LiDEC^+_{el} \rightleftharpoons LiEC^+_{el} + DEC_{el}$	1.98E+08
H61	$EC_{el} + LiDMC^+_{el} \rightleftharpoons LiEC^+_{el} + DMC_{el}$	1.98E+08
H62	$EC_{el} + LiEMC^+_{el} \rightleftharpoons LiEC^+_{el} + EMC_{el}$	1.98E+08
H63	$EC_{el} + LiPC^+_{el} \rightleftharpoons LiEC^+_{el} + PC_{el}$	1.98E+08
H64	$EC_{el} + LiVC^+_{el} \rightleftharpoons LiEC^+_{el} + VC_{el}$	1.98E+08
H65	$EC_{el} + LiBC^+_{el} \rightleftharpoons LiEC^+_{el} + BC_{el}$	1.98E+08
H66	$LiEC^+_{el} + FEC_{el} \rightleftharpoons EC_{el} + LiFEC^+_{el}$	1.98E+08
H67	$LiEC^+_{el} + CO_{2el} \rightleftharpoons EC_{el} + LiCO_2^{+}{}_{el}$	1.98E+08
H68	$EC_{el} + LEDC_{el} \rightleftharpoons LiEC^+_{el} + LEDC\_lessLi_{el}$	1.98E+08
H69	$EC_{el} + Li_2CO_{3el} \rightleftharpoons LiEC^+_{el} + LiCO_3^{-}{}_{el}$	1.98E+08
H70	$LiEC^+_{el} + CH_3CH_2OCO_{el} \rightleftharpoons EC_{el} + LiCH_3CH_2OCO^+_{el}$	1.98E+08
H71	$LiEC^+_{el} + CH_3OCO_{el} \rightleftharpoons EC_{el} + LiCH_3OCO^+_{el}$	1.98E+08
H72	$LiEC^+_{el} + FEC\_lessH_{el} \rightleftharpoons EC_{el} + LiFEC\_lessH^+_{el}$	1.98E+08
H73	$LiDEC^+_{el} + DMC_{el} \rightleftharpoons DEC_{el} + LiDMC^+_{el}$	1.98E+08
H74	$LiDEC^+_{el} + EMC_{el} \rightleftharpoons DEC_{el} + LiEMC^+_{el}$	1.98E+08
H75	$DEC_{el} + LiPC^+_{el} \rightleftharpoons LiDEC^+_{el} + PC_{el}$	1.98E+08
H76	$LiDEC^+_{el} + VC_{el} \rightleftharpoons DEC_{el} + LiVC^+_{el}$	1.98E+08
H77	$DEC_{el} + LiBC^+_{el} \rightleftharpoons LiDEC^+_{el} + BC_{el}$	1.98E+08
H78	$LiDEC^+_{el} + FEC_{el} \rightleftharpoons DEC_{el} + LiFEC^+_{el}$	1.98E+08
H79	$LiDEC^+_{el} + CO_{2el} \rightleftharpoons DEC_{el} + LiCO_2^{+}{}_{el}$	1.98E+08
H80	$DEC_{el} + LEDC_{el} \rightleftharpoons LiDEC^+_{el} + LEDC\_lessLi_{el}$	1.98E+08
H81	$DEC_{el} + Li_2CO_{3el} \rightleftharpoons LiDEC^+_{el} + LiCO_3^{-}{}_{el}$	1.98E+08
H82	$LiDEC^+_{el} + CH_3CH_2OCO_{el} \rightleftharpoons DEC_{el} + LiCH_3CH_2OCO^+_{el}$	1.98E+08
H83	$LiDEC^+_{el} + CH_3OCO_{el} \rightleftharpoons DEC_{el} + LiCH_3OCO^+_{el}$	1.98E+08
H84	$LiDEC^+_{el} + FEC\_lessH_{el} \rightleftharpoons DEC_{el} + LiFEC\_lessH^+_{el}$	1.98E+08
H85	$DMC_{el} + LiEMC^+_{el} \rightleftharpoons LiDMC^+_{el} + EMC_{el}$	1.98E+08
H86	$DMC_{el} + LiPC^+_{el} \rightleftharpoons LiDMC^+_{el} + PC_{el}$	1.98E+08
H87	$LiDMC^+_{el} + VC_{el} \rightleftharpoons DMC_{el} + LiVC^+_{el}$	1.98E+08
H88	$DMC_{el} + LiBC^+_{el} \rightleftharpoons LiDMC^+_{el} + BC_{el}$	1.98E+08
H89	$LiDMC^+_{el} + FEC_{el} \rightleftharpoons DMC_{el} + LiFEC^+_{el}$	1.98E+08
H90	$LiDMC^+_{el} + CO_{2el} \rightleftharpoons DMC_{el} + LiCO_2^{+}{}_{el}$	1.98E+08
H91	$DMC_{el} + LEDC_{el} \rightleftharpoons LiDMC^+_{el} + LEDC\_lessLi_{el}$	1.98E+08
H92	$DMC_{el} + Li_2CO_{3el} \rightleftharpoons LiDMC^+_{el} + LiCO_3^{-}{}_{el}$	1.98E+08
H93	$LiDMC^+_{el} + CH_3CH_2OCO_{el} \rightleftharpoons DMC_{el} + LiCH_3CH_2OCO^+_{el}$	1.98E+08
H94	$LiDMC^+_{el} + CH_3OCO_{el} \rightleftharpoons DMC_{el} + LiCH_3OCO^+_{el}$	1.98E+08
H95	$LiDMC^+_{el} + FEC\_lessH_{el} \rightleftharpoons DMC_{el} + LiFEC\_lessH^+_{el}$	1.98E+08
H96	$EMC_{el} + LiPC^+_{el} \rightleftharpoons LiEMC^+_{el} + PC_{el}$	1.98E+08
H97	$LiEMC^+_{el} + VC_{el} \rightleftharpoons EMC_{el} + LiVC^+_{el}$	1.98E+08
H98	$EMC_{el} + LiBC^+_{el} \rightleftharpoons LiEMC^+_{el} + BC_{el}$	1.98E+08
H99	$LiEMC^+_{el} + FEC_{el} \rightleftharpoons EMC_{el} + LiFEC^+_{el}$	1.98E+08
H100	$LiEMC^+_{el} + CO_{2el} \rightleftharpoons EMC_{el} + LiCO_2^{+}{}_{el}$	1.98E+08
H101	$EMC_{el} + LEDC_{el} \rightleftharpoons LiEMC^+_{el} + LEDC\_lessLi_{el}$	1.98E+08
H102	$EMC_{el} + Li_2CO_{3el} \rightleftharpoons LiEMC^+_{el} + LiCO_3^{-}{}_{el}$	1.98E+08
H103	$LiEMC^+_{el} + CH_3CH_2OCO_{el} \rightleftharpoons EMC_{el} + LiCH_3CH_2OCO^+_{el}$	1.98E+08
H104	$LiEMC^+_{el} + CH_3OCO_{el} \rightleftharpoons EMC_{el} + LiCH_3OCO^+_{el}$	1.98E+08
H105	$LiEMC^+_{el} + FEC\_lessH_{el} \rightleftharpoons EMC_{el} + LiFEC\_lessH^+_{el}$	1.98E+08
H106	$LiPC^+_{el} + VC_{el} \rightleftharpoons PC_{el} + LiVC^+_{el}$	1.98E+08
H107	$LiPC^+_{el} + BC_{el} \rightleftharpoons PC_{el} + LiBC^+_{el}$	1.98E+08
H108	$LiPC^+_{el} + FEC_{el} \rightleftharpoons PC_{el} + LiFEC^+_{el}$	1.98E+08
H109	$LiPC^+_{el} + CO_{2el} \rightleftharpoons PC_{el} + LiCO_2^{+}{}_{el}$	1.98E+08
H110	$PC_{el} + LEDC_{el} \rightleftharpoons LiPC^+_{el} + LEDC\_lessLi_{el}$	1.98E+08
H111	$PC_{el} + Li_2CO_{3el} \rightleftharpoons LiPC^+_{el} + LiCO_3^{-}{}_{el}$	1.98E+08
H112	$LiPC^+_{el} + CH_3CH_2OCO_{el} \rightleftharpoons PC_{el} + LiCH_3CH_2OCO^+_{el}$	1.98E+08
H113	$LiPC^+_{el} + CH_3OCO_{el} \rightleftharpoons PC_{el} + LiCH_3OCO^+_{el}$	1.98E+08
H114	$LiPC^+_{el} + FEC\_lessH_{el} \rightleftharpoons PC_{el} + LiFEC\_lessH^+_{el}$	1.98E+08
H115	$VC_{el} + LiBC^+_{el} \rightleftharpoons LiVC^+_{el} + BC_{el}$	1.98E+08
H116	$LiVC^+_{el} + FEC_{el} \rightleftharpoons VC_{el} + LiFEC^+_{el}$	1.98E+08
H117	$LiVC^+_{el} + CO_{2el} \rightleftharpoons VC_{el} + LiCO_2^{+}{}_{el}$	1.98E+08
H118	$VC_{el} + LEDC_{el} \rightleftharpoons LiVC^+_{el} + LEDC\_lessLi_{el}$	1.98E+08
H119	$VC_{el} + Li_2CO_{3el} \rightleftharpoons LiVC^+_{el} + LiCO_3^{-}{}_{el}$	1.98E+08
H120	$LiVC^+_{el} + CH_3CH_2OCO_{el} \rightleftharpoons VC_{el} + LiCH_3CH_2OCO^+_{el}$	1.98E+08
H121	$LiVC^+_{el} + CH_3OCO_{el} \rightleftharpoons VC_{el} + LiCH_3OCO^+_{el}$	1.98E+08
H122	$LiVC^+_{el} + FEC\_lessH_{el} \rightleftharpoons VC_{el} + LiFEC\_lessH^+_{el}$	1.98E+08
H123	$LiBC^+_{el} + FEC_{el} \rightleftharpoons BC_{el} + LiFEC^+_{el}$	1.98E+08
H124	$LiBC^+_{el} + CO_{2el} \rightleftharpoons BC_{el} + LiCO_2^{+}{}_{el}$	1.98E+08
H125	$BC_{el} + LEDC_{el} \rightleftharpoons LiBC^+_{el} + LEDC\_lessLi_{el}$	1.98E+08
H126	$BC_{el} + Li_2CO_{3el} \rightleftharpoons LiBC^+_{el} + LiCO_3^{-}{}_{el}$	1.98E+08
H127	$LiBC^+_{el} + CH_3CH_2OCO_{el} \rightleftharpoons BC_{el} + LiCH_3CH_2OCO^+_{el}$	1.98E+08
H128	$LiBC^+_{el} + CH_3OCO_{el} \rightleftharpoons BC_{el} + LiCH_3OCO^+_{el}$	1.98E+08
H129	$LiBC^+_{el} + FEC\_lessH_{el} \rightleftharpoons BC_{el} + LiFEC\_lessH^+_{el}$	1.98E+08
H130	$LiFEC^+_{el} + CO_{2el} \rightleftharpoons FEC_{el} + LiCO_2^{+}{}_{el}$	1.98E+08
H131	$FEC_{el} + LEDC_{el} \rightleftharpoons LiFEC^+_{el} + LEDC\_lessLi_{el}$	1.98E+08
H132	$FEC_{el} + Li_2CO_{3el} \rightleftharpoons LiFEC^+_{el} + LiCO_3^{-}{}_{el}$	1.98E+08
H133	$LiFEC^+_{el} + CH_3CH_2OCO_{el} \rightleftharpoons FEC_{el} + LiCH_3CH_2OCO^+_{el}$	1.98E+08
H134	$LiFEC^+_{el} + CH_3OCO_{el} \rightleftharpoons FEC_{el} + LiCH_3OCO^+_{el}$	1.98E+08
H135	$LiFEC^+_{el} + FEC\_lessH_{el} \rightleftharpoons FEC_{el} + LiFEC\_lessH^+_{el}$	1.98E+08
H136	$CO_{2el} + LEDC_{el} \rightleftharpoons LiCO_2^{+}{}_{el} + LEDC\_lessLi_{el}$	1.98E+08
H137	$CO_{2el} + Li_2CO_{3el} \rightleftharpoons LiCO_2^{+}{}_{el} + LiCO_3^{-}{}_{el}$	1.98E+08
H138	$CO_{2el} + LiCH_3CH_2OCO^+_{el} \rightleftharpoons LiCO_2^{+}{}_{el} + CH_3CH_2OCO_{el}$	1.98E+08
H139	$CO_{2el} + LiCH_3OCO^+_{el} \rightleftharpoons LiCO_2^{+}{}_{el} + CH_3OCO_{el}$	1.98E+08
H140	$CO_{2el} + LiFEC\_lessH^+_{el} \rightleftharpoons LiCO_2^{+}{}_{el} + FEC\_lessH_{el}$	1.98E+08
H141	$LEDC\_lessLi_{el} + Li_2CO_{3el} \rightleftharpoons LEDC_{el} + LiCO_3^{-}{}_{el}$	1.98E+08
H142	$LEDC_{el} + CH_3CH_2OCO_{el} \rightleftharpoons LEDC\_lessLi_{el} + LiCH_3CH_2OCO^+_{el}$	1.98E+08
H143	$LEDC_{el} + CH_3OCO_{el} \rightleftharpoons LEDC\_lessLi_{el} + LiCH_3OCO^+_{el}$	1.98E+08
H144	$LEDC_{el} + FEC\_lessH_{el} \rightleftharpoons LEDC\_lessLi_{el} + LiFEC\_lessH^+_{el}$	1.98E+08
H145	$Li_2CO_{3el} + CH_3CH_2OCO_{el} \rightleftharpoons LiCO_3^{-}{}_{el} + LiCH_3CH_2OCO^+_{el}$	1.98E+08
H146	$Li_2CO_{3el} + CH_3OCO_{el} \rightleftharpoons LiCO_3^{-}{}_{el} + LiCH_3OCO^+_{el}$	1.98E+08
H147	$Li_2CO_{3el} + FEC\_lessH_{el} \rightleftharpoons LiCO_3^{-}{}_{el} + LiFEC\_lessH^+_{el}$	1.98E+08
H148	$LiCH_3CH_2OCO^+_{el} + CH_3OCO_{el} \rightleftharpoons CH_3CH_2OCO_{el} + LiCH_3OCO^+_{el}$	1.98E+08
H149	$CH_3CH_2OCO_{el} + LiFEC\_lessH^+_{el} \rightleftharpoons LiCH_3CH_2OCO^+_{el} + FEC\_lessH_{el}$	1.98E+08

Figure S1: Predicted selected electrolyte species concentrations during a 100 mV voltage hold. Responses are shown every 30 hr during the hold.

S2. Nondimensionalization and finite-differencing

The code is found to be particularly unstable when considering complex reaction mechanisms. This is probably due to the ridiculous concentration disparity between internal variable tracked by the solver. To remedy this issue, the independent variables are non-dimensionalized in such a way as to make the solver more stable. The following nondimensional terms are introduced to the governing equations:

$$\left[\hat{X}_k\right] = \Gamma_k\left[X_k\right], \quad \hat{\phi} = \Gamma_\phi\phi, \quad \hat{\delta} = \Gamma_\delta\delta, \tag{S1}$$

where the $\hat{}$ indicates the scaled variable, and Γ_k, Γ_Φ, and Γ_δ are scaling factors. Note that because there is significant disparity between concentrations of minor, intermediate species and major species, Γ_k is species dependent. The governing equations for the rescaled system are expressed as

$$\frac{\partial[X_k]}{\partial\tau} + \left(\frac{-\zeta}{\delta}\frac{\partial[X_k]}{\partial\zeta}\right)\frac{\partial\delta}{\partial\tau} = \frac{1}{\delta r^2}\frac{\partial}{\partial\zeta}\left(\frac{r^2 D_k}{\delta}\frac{\partial[X_k]}{\partial\zeta} + \frac{r^2 D_k}{\delta}\frac{z_k F[X_k]}{RT}\frac{\partial\Phi}{\partial\zeta}\right) + \dot{\omega}_k, \tag{S2}$$

$$\frac{1}{\Gamma_k}\frac{\partial[\hat{X}_k]}{\partial t} + \frac{1}{\Gamma_k}\left(\frac{-\zeta}{\hat{\delta}}\frac{\partial[\hat{X}_k]}{\partial\zeta}\right)\frac{\partial\hat{\delta}}{\partial\tau} = \Gamma_\delta^2\frac{1}{\hat{\delta}r^2}\frac{\partial}{\partial\zeta}\left(\frac{r^2 D_k}{\hat{\delta}}\frac{\partial[\hat{X}_k]}{\partial\zeta}\frac{1}{\Gamma_k} + \frac{r^2 D_k}{\hat{\delta}}\frac{z_k F[\hat{X}_k]}{RT}\frac{\partial\hat{\Phi}}{\partial\zeta}\frac{1}{\Gamma_k\Gamma_\phi}\right) + \dot{\omega}_k, \tag{S3}$$

$$\frac{\partial[\hat{X}_k]}{\partial\tau} + \left(\frac{-\zeta}{\hat{\delta}}\frac{\partial[\hat{X}_k]}{\partial\zeta}\right)\frac{\partial\hat{\delta}}{\partial\tau} = \Gamma_\delta^2\frac{1}{\hat{\delta}r^2}\frac{\partial}{\partial\zeta}\left(\frac{r^2 D_k}{\hat{\delta}}\frac{\partial[\hat{X}_k]}{\partial\zeta} + \frac{r^2 D_k}{\hat{\delta}}\frac{z_k F[\hat{X}_k]}{RT}\frac{\partial\hat{\Phi}}{\partial\zeta}\frac{1}{\Gamma_\phi}\right) + \dot{\omega}_k\Gamma_k. \tag{S4}$$

It should be noted that the volumetric production rate $\dot{\omega}_k$ relies on the unscaled values, not the scaled values. Unscaled values also need to be used for surface reactions at the SEI/electrolyte interface, and to compute the radial term r. Note that $r = \zeta\delta + r_{\mathrm{p}}$, or in a scaled version: $r = \zeta\hat{\delta}/\Gamma_\delta + r_{\mathrm{p}}$.

Considering the finite volume differencing scheme, the right side of the conservation of species equation (i.e., f in $My' = f(t, y; p)$) for the scaled system is

$$\hat{f}_k = \Gamma_\delta^2\frac{1}{\hat{\delta}r^2}\frac{\partial}{\partial\zeta}\left(\frac{r^2 D_k}{\hat{\delta}}\frac{\partial[\hat{X}_k]}{\partial\zeta} + \frac{r^2 D_k}{\hat{\delta}}\frac{z_k F[\hat{X}_k]}{RT}\frac{\partial\hat{\Phi}}{\partial\zeta}\frac{1}{\Gamma_\phi}\right) + \dot{\omega}_k\Gamma_k, \tag{S5}$$

$$\hat{f}_k = \Gamma_\delta^2\frac{1}{\hat{\delta}r_j^2}\frac{1}{\zeta_{j+1/2} - \zeta_{j-1/2}}\left(\frac{r_{j+1/2}^2 D_k}{\hat{\delta}}\frac{[\hat{X}_k]_{j+1} - [\hat{X}_k]_j}{\zeta_{j+1} - \zeta_j} - \frac{r_{j-1/2}^2 D_k}{\hat{\delta}}\frac{[\hat{X}_k]_j - [\hat{X}_k]_{j-1}}{\zeta_j - \zeta_{j-1}}\right.$$
$$\left. + \left[\frac{r_{j+1/2}^2 D_k}{\hat{\delta}}\frac{z_k F[\hat{X}_{k\,j+1/2}]}{RT}\frac{\hat{\Phi}_{j+1} - \hat{\Phi}_j}{\zeta_{j+1} - \zeta_j} - \frac{r_{j-1/2}^2 D_k}{\hat{\delta}}\frac{z_k F[\hat{X}_{k\,j-1/2}]}{RT}\frac{\hat{\Phi}_j - \hat{\Phi}_{j-1}}{\zeta_j - \zeta_{j-1}}\right]\frac{1}{\Gamma_\phi}\right) + \dot{\omega}_k\Gamma_k, \tag{S6}$$

Rearranging and writing in a more compact form results in

$$\hat{f}_k = -\Gamma_\delta\frac{1}{\hat{\delta}r_j^2}\frac{1}{\zeta_{j+1/2} - \zeta_{j-1/2}}\left(r_{j+1/2}^2\hat{J}_{k,j+1/2} - r_{j-1/2}^2\hat{J}_{k,j-1/2}\right) + \dot{\omega}_k\Gamma_k,$$

$$\hat{J}_{k,j+1/2} = \Gamma_\delta\left(-\frac{D_k}{\hat{\delta}}\frac{[\hat{X}_k]_{j+1} - [\hat{X}_k]_j}{\zeta_{j+1} - \zeta_j} - \frac{D_k}{\hat{\delta}}\frac{z_k F[\hat{X}_{k\,j+1/2}]}{RT}\frac{\hat{\Phi}_{j+1} - \hat{\Phi}_j}{\zeta_{j+1} - \zeta_j}\frac{1}{\Gamma_\phi}\right), \tag{S7}$$

$$\hat{J}_{k,j-1/2} = \Gamma_\delta\left(-\frac{D_k}{\hat{\delta}}\frac{[\hat{X}_k]_j - [\hat{X}_k]_{j-1}}{\zeta_j - \zeta_{j-1}} - \frac{D_k}{\hat{\delta}}\frac{z_k F[\hat{X}_{k\,j-1/2}]}{RT}\frac{\hat{\Phi}_j - \hat{\Phi}_{j-1}}{\zeta_j - \zeta_{j-1}}\frac{1}{\Gamma_\phi}\right).$$

A similar approach is used for non-dimensionalizing electroneutrality

$$\sum_k z_k\frac{\partial[X_k]}{\partial\tau} = 0, \tag{S8}$$

$$\sum_k \frac{z_k}{\Gamma_k} \frac{\partial [\hat{X}_k]}{\partial \tau} = 0. \tag{S9}$$

Note that since Γ_k is species-specific, the Γ_k terms can not be pulled out of the summations.

The SEI growth rate can be scaled as

$$\frac{\partial \delta}{\partial \tau} = \sum_{k,\text{struct}} \frac{W_k}{\rho_k} \dot{s}_k, \tag{S10}$$

$$\frac{1}{\Gamma_\delta} \frac{\partial \hat{\delta}}{\partial \tau} = \sum_{k,\text{struct}} \frac{W_k}{\rho_k} \dot{s}_k \left(\frac{\left[\hat{X}_k \right]}{\Gamma_k} + [X_k]_0, \frac{\hat{\Phi}}{\Gamma_\phi} \right), \tag{S11}$$

$$\frac{\partial \hat{\delta}}{\partial \tau} = \Gamma_\delta \sum_{k,\text{struct}} \frac{W_k}{\rho_k} \dot{s}_k \left(\frac{\left[\hat{X}_k \right]}{\Gamma_k} + [X_k]_0, \frac{\hat{\Phi}}{\Gamma_\phi} \right) = \Gamma_\delta \sum_{k,\text{struct}} \Gamma_k \frac{W_k}{\rho_k} \hat{s}_k, \tag{S12}$$

As a numerical trick δ is solved throughout the domain. If δ is solved somewhere other than the SEI/electrolyte surface node, then the governing equation is

$$\frac{\partial \delta_j}{\partial \tau} = \frac{\partial \delta_{j+1}}{\partial \tau}, \tag{S13}$$

where, j is the cell number. Rescaling these equations results in

$$\frac{\partial \hat{\delta}_j}{\partial \tau} = \frac{\partial \hat{\delta}_{j+1}}{\partial \tau}. \tag{S14}$$

Finally, conservation of lattice sites results in

$$\frac{\partial \left[\text{Li}^0_{\text{SEI}} \right]}{\partial \tau} + \frac{\partial \left[\text{V}^-_{\text{SEI}} \right]}{\partial \tau} = 0, \tag{S15}$$

$$\frac{1}{\Gamma_{\text{Li}^0_{\text{SEI}}}} \frac{\partial \left[\hat{\text{Li}}^0_{\text{SEI}} \right]}{\partial t} + \frac{1}{\Gamma_{\text{V}^-_{\text{SEI}}}} \frac{\partial \left[\hat{\text{V}}^-_{\text{SEI}} \right]}{\partial t} = 0. \tag{S16}$$

Note that since $\Gamma_{\text{Li}^0_{\text{SEI}}}$ and $\Gamma_{\text{V}^-_{\text{SEI}}}$ are not necessarily equal, they are not cancelled out.

S2.1. Boundary nodes

There are four control volumes in the system that are not interior nodes. These nodes are 1) the SEI node at the anode interface (the first node), 2) the last SEI node at the electrolyte interface, 3) the first electrolyte node at the SEI interface, and 4) the furthest electrolyte node at the edge of the simulation domain. These boundary nodes require special consideration.

For the first SEI control volume, the species concentration is assumed to be constant (in radial space). This can be expressed mathematically as

$$\frac{\partial [X_k]}{\partial t} = 0. \tag{S17}$$

Note, that in the radial domain, there is no velocity. However, in the transformed domain, there is a velocity due to the uniform stretch, which appears as another term relying on the change in SEI thickness. Using the Landau transformation, this can be expressed in the transformed domain as

$$\frac{\partial [X_k]}{\partial \tau} + \left(\frac{-\zeta}{\delta} \frac{\partial [X_k]}{\partial \zeta} \right) \frac{\partial \delta}{\partial \tau} = 0. \tag{S18}$$

This governing equation can be solved using a finite-difference method in the ζ coordinate as

$$\frac{\partial [X_k]_j}{\partial \tau} + \left(\frac{-\zeta_j}{\delta_j} \frac{[X_k]_{j+1} - [X_k]_j}{\zeta_{j+1} - \zeta_j} \right) \frac{\partial \delta}{\partial \tau} = 0. \tag{S19}$$

7

where subscript j indicates that the node number (which is unity for this case). In scaled terms, the governing equation can be expressed as

$$\frac{\partial [\hat{X}_k]_j}{\partial \tau} + \left(\frac{-\zeta_j}{\hat{\delta}_j} \frac{[\hat{X}_k]_{j+1} - [\hat{X}_k]_j}{\zeta_{j+1} - \zeta_j} \right) \frac{\partial \hat{\delta}}{\partial \tau} = 0. \tag{S20}$$

At the reactive SEI/electrolyte boundary, the flux is due to surface reactions i.e.,

$$\left(\mathbf{J}_k \cdot \mathbf{n} - [X_k]\frac{\partial \delta}{\partial t} \right) = -\dot{s}_k \Big|_{\zeta=1}, \tag{S21}$$

where $\mathbf{J}_k$ is the species flux, $\mathbf{n}$ is the surface normal, and $\dot{s}_k$ is the surface species production rate. For the special case of the first electrolyte cell next to the SEI, and the last SEI node, one of the surface species flux is governed by surface reactions. Replacing the species flux with net reaction rates of progress changes the governing equation for these nodes. Species conservation can be expressed generally using a finite differencing scheme as

$$\frac{\partial [X_k]_j}{\partial \tau} + \left(\frac{-\zeta_j}{\delta} \frac{\partial [X_k]}{\partial \zeta} \right) \frac{\partial \delta}{\partial \tau} = \frac{-1}{\delta r_j^2} \frac{1}{\zeta_{j+1/2} - \zeta_{j-1/2}} \left(r_{j+1/2}^2 J_{j+1/2} - r_{j-1/2}^2 J_{j-1/2} \right) + \dot{\omega}_k, \tag{S22}$$

where the fluxes J contain the bulk velocity term. For the last SEI control volume, the flux on the positive face is replaced with species reactions. The fluxes for the last SEI node can be expressed as

$$\begin{aligned} J_{k,j+1/2} &= [X_k]_j \frac{\partial \delta}{\partial t} - \dot{s}_k, \\ J_{k,j-1/2} &= -\frac{D_k}{\delta} \frac{[X_k]_j - [X_k]_{j-1}}{\zeta_j - \zeta_{j-1}} - \frac{D_k}{\delta} \frac{z_k F [X_k]_{j-1/2}}{RT} \frac{\Phi_j - \Phi_{j-1}}{\zeta_j - \zeta_{j-1}}. \end{aligned} \tag{S23}$$

S3. Voltage-hold capacity deconvolution

Irreversible capacity loss estimation during the voltage-hold (V-hold) is described here. Let Q_1, Q_2 and Q_{hold} be the cell's capacity before, after, and during the voltage-hold, respectively. The capacity during voltage-hold Q_{hold} can be represented as the sum of irreversible Q_{irr} and reversible contributions Q_{rev}:

$$Q_{\text{hold}}(t) = Q_{\text{irr}}(t) + Q_{\text{rev}}(t) = at^p + Q_{\text{rev}}^{\text{final}} \frac{(c + t_{\text{final}})t}{t_{\text{final}}(c + t)}, \tag{S24}$$

$$Q_{\text{hold}}|_{t_{\text{final}}} = Q_{\text{irrev}}|_{t_{\text{final}}} + Q_{\text{rev}}|_{t_{\text{final}}}. \tag{S25}$$

The current during the voltage-hold is obtained from the capacity model fit through:

$$i_{\text{hold}}(t) = \frac{dQ_{\text{hold}}(t)}{dt} = \frac{dQ_{\text{irr}}(t)}{dt} + \frac{dQ_{\text{rev}}(t)}{dt} = pat^{p-1} + \frac{Q_{\text{rev}}|_{t_{\text{final}}}(c + t_{\text{final}})c}{t_{\text{final}}(c + t)^2}. \tag{S26}$$

In these expressions, the irreversible capacity Q_{irr} is assumed to be well represented by a power law. Similarly, the reversible capacity Q_{rev} is assumed to have a plateauing behavior of reversible lithiation of Si as the V-hold time increases. The c parameter (in the reversible capacity) has units of time and is physically relevant; it is a measure of reversible lithiation rate of Si during the constant V-hold. A relatively small c indicates fast relaxation of transport and kinetic processes throughout the Si anode particles. Rapid relaxation means that the final reversible capacity $Q_{\text{rev}}|_{t_{\text{final}}}$ is reached early in the voltage hold. In contrast, a relatively high c value indicates that the constant-voltage Si lithiation is a slow process (high impedance, slow transport), which means that reversible lithiation may still be active even after t_{final}. In the capacity fit, there are four unknown parameters, a, p, $Q_{\text{rev}}|_{t_{\text{final}}}$, and c. In principle, these parameters can be fit to the measured data to accurately deconvolve irreversible and reversible capacity from the measured current during the V-hold. However, using four unknown parameters to fit the measured current relaxation profiles can result in over-fitting.
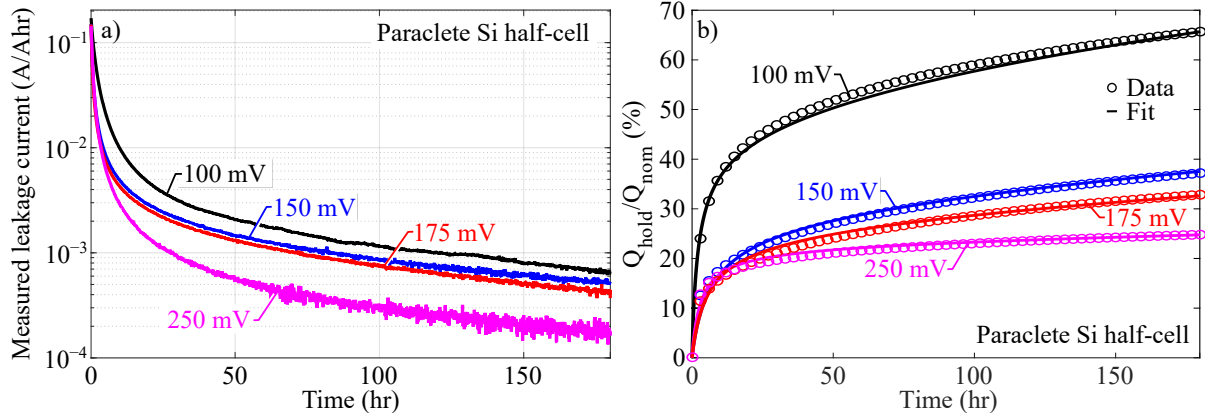
8

Figure S2: Measured leakage current during 180 hr voltage hold (before deconvolution).

To reduce the number of unknown parameters, the reversible capacity $Q_{\text{rev}}^{\text{final}}$ is determined by subtracting the cell's capacity before (Q_1) and after (Q_2) the hold:

$$Q_{\text{rev}}|_{t_{\text{final}}} = Q_2 - Q_1. \tag{S27}$$

To further reduce the number of unknown parameters, the irreversible current exponent is first assumed to be $p = 0.5$ (i.e., a diffusion-limited case), and a and c are used as fitting parameters. If a good fit ($R^2 > 0.99$) is not found with assuming $p = 0.5$, then all three parameters (a, c, p) are used to fit the response. The optimization problem is solved using MATLAB's curve fitting toolbox. The objective function can be stated as finding a, c, with $p = 0.5$ such that Eq. S24- S27 are satisfied. If $p = 0.5$ does not accurately fit the data, p is also used as a fitting parameter. The parameter bounds are set as: $a : (0, 5)$, $c : (0, 100)$, and $p : (0.3, 1)$.

Figures S2(a) and S2(b) show the measured leakage currents in the Li-Si half cell experiment and the corresponding deconvolution model fits for the total hold capacity, respectively. Leakage currents and capacity are normalized with the nominal discharge capacity before the hold Q_{norm} to standardize comparison between cells. For all tests, the leakage current decreases with respect to time.

Table S5: Leakage current best fit model parameters

Parameter	100 mV	150 mV	175 mV	250 mV
a	3.19	1.33	0.78	0.25
p	0.45	0.50	0.54	0.55
c	5	6	5	3
$Q_{\text{rev}}^{\text{final}}$ (%)	32.65	19.70	19.72	20.41
t_{final} (hr)	180	180	180	180

Model fits for normalized hold capacity in Fig. S2(b) show agreement with experimental data ($R^2 > 0.99$). Capacity exchanged during the hold mirrors the current trend, i.e., 100 mV > 150 mV > 175 mV > 250 mV. Table S5 documents the deconvolution model fit parameters. Low voltage holds are associated with higher magnitudes of a for relatively similar values of p indicating faster irreversible SEI capacity growth at high Si state of charge. Of the total hold capacity, reversible capacity proportion is highest for 100 mV. Timescale of reversible capacity growth c is similar for 100 mV - 175 mV holds indicating sluggish lithiation kinetics at high SOCs.

S4. Electrolyte transformed domain

The electrolyte domain is transformed separately from the SEI domain. In the electrolyte domain, the spatial coordinate r is transformed to a moving boundary ξ domain. The ξ domain starts at the SEI/electrolyte interface (i.e., $r = r_p + \delta$) and ends at a fixed boundary far away from the particle (at $r = R_{el}$). The transformed variable can be expressed in terms of radius as

$$\xi = \frac{r - r_p - \delta}{R_{el} - r_p - \delta}. \tag{S28}$$

Similarly to the SEI transformation of variables, the respective derivatives for ξ can be expressed as

$$\left(\frac{\partial \xi}{\partial r}\right)_t = \frac{1}{R_{el} - r_p - \delta}, \tag{S29}$$

$$\left(\frac{\partial \xi}{\partial t}\right)_r = \frac{\xi - 1}{R_{el} - r_p - \delta} \frac{\partial \delta}{\partial t}. \tag{S30}$$

Note: ζ is used to transform the SEI domain to a moving boundary formulation, where the domain spans from $r_p \leq r \leq r_p + \delta(t)$. In the electrolyte transformation, ξ is the independent variable, which spans from $r_p + \delta(t) \leq r \leq R_{el}$, where R_{el} is time invariant.

A coordinate transformation is used to solve the governing equation on a fixed mesh (in the electrolyte domain) [61, 75, 76]. For this particular transformation (Note: $t = \tau$), the respective partial derivates result in

$$\left(\frac{\partial A}{\partial r}\right)_t = \frac{1}{R_{el} - r_p - \delta} \left(\frac{\partial A}{\partial \xi}\right)_\tau, \tag{S31}$$

$$\left(\frac{\partial A}{\partial t}\right)_r = \frac{\xi - 1}{R_{el} - r_p - \delta} \frac{\partial \delta}{\partial \tau} \left(\frac{\partial A}{\partial \xi}\right)_\tau + \left(\frac{\partial A}{\partial \tau}\right)_\xi. \tag{S32}$$

In the original spatial domain, species conservation can be expressed as

$$\frac{\partial [X_k]}{\partial t} = \frac{1}{r^2} \frac{\partial}{\partial r} \left(r^2 D_k \frac{\partial [X_k]}{\partial r} + r^2 D_k \frac{z_k F [X_k]}{RT} \frac{\partial \Phi}{\partial r}\right) + \dot{\omega}_k. \tag{S33}$$

Using the electrolyte domain transformation results in

$$\frac{\partial [X_k]}{\partial \tau} + \left(\frac{\xi - 1}{R_{el} - r_p - \delta} \frac{\partial [X_k]}{\partial \xi}\right) \frac{\partial \delta}{\partial \tau} = \frac{1}{\left(R_{el} - r_p - \delta\right)^2 r^2} \frac{\partial}{\partial \xi} \left(r^2 D_k \frac{\partial [X_k]}{\partial \xi} + r^2 D_k \frac{z_k F [X_k]}{RT} \frac{\partial \Phi}{\partial \xi}\right) + \dot{\omega}_k. \tag{S34}$$

For comparison, conservation in the SEI domain is expressed in the ζ domain as

$$\frac{\partial [X_k]}{\partial \tau} + \left(\frac{-\zeta}{\delta} \frac{\partial [X_k]}{\partial \zeta}\right) \frac{\partial \delta}{\partial \tau} = \frac{1}{\delta^2 r^2} \frac{\partial}{\partial \zeta} \left(r^2 D_k \frac{\partial [X_k]}{\partial \zeta} + r^2 D_k \frac{z_k F [X_k]}{RT} \frac{\partial \Phi}{\partial \zeta}\right) + \dot{\omega}_k. \tag{S35}$$

There is some care needed for the re-scaled version of the electrolyte transformed equations since there is fewer convenient cancellations. The scaled version can be simplified as

$$\frac{1}{\Gamma_k} \frac{\partial [\hat{X}_k]}{\partial \tau} + \frac{1}{\Gamma_k \Gamma_\delta} \left(\frac{\xi - 1}{R_{el} - r_p - \hat{\delta}/\Gamma_\delta} \frac{\partial [\hat{X}_k]}{\partial \xi}\right) \frac{\partial \hat{\delta}}{\partial \tau} = \frac{1}{\left(R_{el} - r_p - \hat{\delta}/\Gamma_\delta\right)^2 r^2} \frac{\partial}{\partial \xi} \left(\frac{r^2 D_k}{\Gamma_k} \frac{\partial [\hat{X}_k]}{\partial \xi} + \frac{r^2 D_k}{\Gamma_k \Gamma_\phi} \frac{z_k F [\hat{X}_k]}{RT} \frac{\partial \hat{\Phi}}{\partial \xi}\right) + \dot{\omega}_k, \tag{S36}$$

$$\frac{\partial [\hat{X}_k]}{\partial \tau} + \left(\frac{\xi - 1}{\Gamma_\delta R_{el} - \Gamma_\delta r_p - \hat{\delta}} \frac{\partial [\hat{X}_k]}{\partial \xi}\right) \frac{\partial \hat{\delta}}{\partial \tau} = \frac{1}{\left(R_{el} - r_p - \hat{\delta}/\Gamma_\delta\right)^2 r^2} \frac{\partial}{\partial \xi} \left(r^2 D_k \frac{\partial [\hat{X}_k]}{\partial \xi} + \frac{r^2 D_k}{\Gamma_\phi} \frac{z_k F [\hat{X}_k]}{RT} \frac{\partial \hat{\Phi}}{\partial \xi}\right) + \Gamma_k \dot{\omega}_k. \tag{S37}$$